

Predictions for Herschel from Λ CDM: unveiling the cosmic star formation history

C. G. Lacey ^{*},¹ C. M. Baugh,¹ C.S. Frenk,¹ A.J. Benson,² A. Orsi,¹
L. Silva,³ G.L. Granato,³ and A. Bressan,⁴

¹*Institute for Computational Cosmology, Department of Physics, University of Durham, South Road, Durham, DH1 3LE, UK*

²*MC350-17, California Institute of Technology, Pasadena, CA 91125, USA*

³*INAF, Osservatorio Astronomico di Trieste, Via Tiepolo 11, I-34131 Trieste, Italy*

⁴*INAF, Osservatorio Astronomico di Padova, Vicolo dell'Osservatorio 2, I-35122 Padova, Italy.*

31 October 2021

ABSTRACT

We use a model for the evolution of galaxies in the far-IR based on the Λ CDM cosmology to make detailed predictions for upcoming cosmological surveys with the *Herschel* Space Observatory. We use the combined GALFORM semi-analytical galaxy formation model and GRASIL spectrophotometric code to compute galaxy SEDs including the reprocessing of radiation by dust. The model, which is the same as that in Baugh et al. (2005), assumes two different IMFs: a normal solar neighbourhood IMF for quiescent star formation in disks, and a very top-heavy IMF in starbursts triggered by galaxy mergers. We have shown previously that the top-heavy IMF appears necessary to explain the number counts and redshifts of faint sub-mm galaxies. In this paper, we present predictions for galaxy luminosity functions, number counts and redshift distributions in the *Herschel* imaging bands. We find that source confusion will be a serious problem in the deepest planned surveys. We also show predictions for physical properties such as star formation rates and stellar, gas and halo masses, together with fluxes at other wavelengths (from the far-UV to the radio) relevant for multi-wavelength follow-up observations. We investigate what fraction of the total IR emission from dust and of the high-mass star formation over the history of the Universe should be resolved by planned surveys with *Herschel*, and find a fraction $\sim 30 - 50\%$, depending on confusion. Finally, we show that galaxies in *Herschel* surveys should be significantly clustered.

Key words: galaxies: evolution – galaxies: formation – galaxies: high-redshift – infrared: galaxies – ISM: dust, extinction

1 INTRODUCTION

The *Herschel* Space Observatory was launched on 14 May 2009 and will begin science observations towards the end of the year. It will observe the Universe at far-infrared (IR) wavelengths, from 60 to 670 μm , and will be far more sensitive at these wavelengths than any previous telescope. One of its primary goals will be to probe the dust-obscured part of the cosmic history of star formation. In this paper we use a state-of-the-art theoretical model of galaxy formation based on structure formation in the Λ CDM model, combined with a detailed treatment of the reprocessing of stellar radiation to far-IR wavelengths, to make predictions for what should be seen in cosmological surveys with *Herschel*, and for how well *Herschel* should be able to achieve its goal of unveiling the cosmic star formation history.

The *Herschel* satellite follows in a line of previous space-based IR telescopes, starting in the 1980s and 1990s with *IRAS*

and *ISO* and including most recently *Spitzer* and *AKARI*. These have gradually revealed the nature and evolution of the galaxy population at mid- and far-IR wavelengths which are inaccessible from the ground, where galaxy luminosities are dominated by emission from interstellar dust grains (see reviews by Soifer et al. 1987; Elbaz 2005; Soifer et al. 2008). More recently, these observations from space have been complemented by surveys at longer, sub-mm wavelengths from the ground, starting with surveys at 850 μm using the *SCUBA* instrument on the *JCMT* (Smail et al. 1997; Hughes et al. 1998). However, due to their poor sensitivities and angular resolutions at these wavelengths, these earlier space missions provided only very limited direct information on the evolution of galaxies in the rest-frame far-IR range which contains most of the energy re-radiated from dust grains heated by starlight. The ground-based sub-mm surveys have also been limited to seeing only the very highest luminosity galaxies at high redshifts, and have been hampered by the fact that they only observe dust emission longwards of the peak in the spectral energy distribution (SED). *Herschel* will, for the first time, allow observations of galaxy SEDs

* E-mail: Cedric.Lacey@durham.ac.uk (CGL)

around the far-IR peak in dust emission out to high redshifts, and thus back to when the Universe was only a fraction of its current age.

Although observations with *IRAS* had already shown that certain types of nearby star-forming galaxies (the Ultra-Luminous IR Galaxies, or ULIRGs) emit most of their luminosity through dust emission in the far-IR (see the review by Soifer et al. 1987), a landmark was achieved with the discovery by *COBE* of the cosmic far-IR background (Puget et al. 1996; Hauser et al. 1998; Fixsen et al. 1998). This far-IR background was found to have an energy density comparable to the ultraviolet (UV)/optical background from stars. The far-IR background is most naturally interpreted as the emission from dust in galaxies heated by starlight, integrated over the history of the Universe. (There is also a contribution to the far-IR background from dust heated by radiation from AGN, but, based on multi-wavelength, especially X-ray, studies, the AGN contribution appears to be small, only $\sim 10\%$ overall (e.g. Almaini et al. 1999; Fardal et al. 2007). Since most of the heating of dust in galaxies is due to radiation from young stars, the far-IR background provides powerful evidence that the bulk of star formation over the history of the Universe has been obscured by dust, with most of the radiation from young stars having been reprocessed from UV to far-IR wavelengths. It is hoped that observations with *Herschel* will allow most of the far-IR background to be directly resolved into individual sources. Preliminary constraints on the far-IR source counts have recently been obtained with the balloon-born BLAST telescope (Devlin et al. 2009), but surveys with *Herschel* will have both better angular resolution and much better sensitivity.

Measuring the cosmic star formation history, and understanding it in terms of physical models for galaxy formation and evolution, are among the main goals of modern cosmology. Observational studies of the cosmic SFR history began with optically-selected samples of galaxies at different redshifts, which typically used the rest-frame UV emission from galaxies as the SFR indicator (Lilly et al. 1996; Madau et al. 1996; Steidel et al. 1999). The earliest studies derived cosmic SFR histories ignoring the effects of dust extinction altogether, but it soon became apparent that this approach was inadequate, since studies of local star-forming galaxies had previously shown that these galaxies usually had appreciable dust extinctions in the rest-frame UV (e.g. Meurer et al. 1995). Applying locally-derived relations between UV extinction and UV spectral slope (Meurer et al. 1995; Calzetti et al. 1995) to high-redshift optically-selected galaxy samples, in particular the Lyman-break galaxies (LBGs), implied that these galaxies should have large UV dust extinctions, and thus also large dust corrections to the SFRs inferred from their rest-frame UV luminosities (Steidel et al. 1999; Meurer et al. 1999). However, in the absence of rest-frame far-IR data on these high-redshift galaxies, which would directly measure the amount of energy absorbed and re-radiated by dust, these corrections for dust extinction remain very uncertain. Correspondingly the cosmic SFR histories derived from dust-corrected rest-frame UV data also have large uncertainties.

There have also been attempts to estimate the cosmic SFR history from sub-mm surveys (e.g. Hughes et al. 1998; Chapman et al. 2005), but here the problems have been that these surveys have detected only small numbers of the most luminous galaxies at high redshift, that the redshifts of many of these are uncertain, and that an extrapolation of the SED must be made from the sub-mm to the far-IR in order to derive the total IR luminosity from dust, from which the SFR is calculated. (In a highly dust-obscured star-forming galaxy, almost all of the UV light from young stars is reprocessed into IR emission by dust, and so the total dust luminosity

provides a good measure of the underlying UV luminosity, and thus of the SFR.) More recently, observations of the mid-IR emission from dust in galaxies have been used to try to infer the cosmic SFR history (e.g. Le Floch et al. 2005; Pérez-González et al. 2005), but this method has the drawback that the SED must be extrapolated from the mid-IR to the far-IR in order to estimate the total dust luminosity. The mid-IR/far-IR ratio is known from nearby examples to show large variations between galaxies, so this extrapolation is likewise uncertain when applied to high-redshift galaxies where there is no direct measurement of the far-IR. Measurements of the cosmic SFR history using *Herschel* will avoid all of the problems associated with these other SFR tracers by measuring the far-IR emission directly.

An important issue which we have not yet discussed is that of the stellar Initial Mass Function (IMF). All of the methods used to estimate observationally the SFRs of high-redshift galaxies (whether from rest-frame UV or IR emission, or emission line or radio luminosities) actually only directly trace *massive* young stars (typically $\gtrsim 5M_{\odot}$), and so really provide measures of the SFR for high-mass stars only. Deriving the total SFR for the whole range of stellar mass ($\sim 0.1 - 100M_{\odot}$) requires an extrapolation using an assumed IMF. It is conventional in observational estimates of the cosmic SFR history to assume a universal IMF, usually taken to be similar to that in the solar neighbourhood. However, this assumption of a universal IMF has no direct observational basis, especially at higher redshifts, and indeed already appears to lead to inconsistencies between estimated cosmic SFR histories and independent estimates of the evolution of the stellar mass density (e.g. Pérez-González et al. 2008). We return to this issue later in the paper.

As already stated, the aim of this paper is to make predictions for what cosmological surveys with *Herschel* should see, based on the best current *ab initio* models both for how galaxies form and evolve, and for how the radiation they emit is distributed over UV, optical, IR and sub-mm wavelengths. Before we discuss our own approach in more detail, we briefly review the different modelling strategies for galaxy evolution in the mid- and far-IR. The models can be broadly divided into two classes, *phenomenological models* and *hierarchical galaxy formation models*. In *phenomenological models*, the galaxy luminosity function (LF) in the IR and its evolution are given by some phenomenological fit, and the IR SEDs are likewise empirical fits, with the parameters in the evolving LF adjusted to match various observational data (e.g. Rowan-Robinson 2001; Lagache et al. 2003; Rowan-Robinson 2009). These models are generally restricted to modelling the dust emission from galaxies, and do not include the UV/optical/near-IR emission from stars. They have been used by e.g. Fernandez-Conde et al. (2008) to make predictions for *Herschel*. In *hierarchical galaxy formation models*, the mass assembly of galaxies is related to structure formation in the dark matter, and star formation and galaxy merger histories are calculated based on physical prescriptions for star formation, supernova feedback, dynamical friction etc. These models typically use theoretical stellar population synthesis models to compute galaxy stellar luminosities, combined with some physical model for the dust extinction, but then can be distinguished according to how they compute the SED of dust emission. Some employ empirical or phenomenological SEDs for the dust (e.g. Devriendt & Guiderdoni 2000); others employ fully theoretical dust SEDs based on radiative transfer and detailed modelling of heating and cooling of dust grains. The modelling approach we use here, which has been set out in Granato et al. (2000), Baugh et al. (2005) and Lacey et al. (2008),

is of the latter type, with detailed physical modelling both of galaxy formation and of the galaxy SEDs. Other models of the same type include Fontanot et al. (2007). We note here some of the advantages of hierarchical galaxy formation models over phenomenological models for galaxy evolution in the IR: they provide a direct link to theoretical models of structure formation; typically they predict galaxy SEDs over a wider wavelength range than the IR, including at least the UV and optical; generally they predict a wide range of other galaxy properties, such as masses, sizes, gas fractions and morphologies; and finally, they allow direct predictions of galaxy clustering, without any further assumptions.

This present paper is the fourth in a series, where we combine the GALFORM semi-analytical model of galaxy formation (Cole et al. 2000) with the GRASIL model for stellar and dust emission from galaxies (Silva et al. 1998). The GALFORM model computes the evolution of galaxies in the framework of the Λ CDM model of structure formation, based on physical treatments of the assembly of dark matter halos by merging, gas cooling in halos, star formation and supernova feedback, galaxy mergers, and chemical enrichment. The GRASIL model computes the SED of a model galaxy from the far-UV to the radio, based on theoretical models of stellar evolution and stellar atmospheres, radiative transfer through a two-phase dust medium to calculate both the dust extinction and dust heating, and a distribution of dust temperatures in each galaxy calculated from a detailed dust grain model.

In the first paper in the series (Granato et al. 2000), we modelled the IR properties of galaxies in the local Universe. While this model was very successful in explaining observations of the local Universe, we found subsequently that it failed when confronted with observations of star-forming galaxies at high redshifts, predicting far too few sub-mm galaxies (SMGs) at $z \sim 2$ and Lyman-break galaxies (LBGs) at $z \sim 3$. Therefore, in the second paper (Baugh et al. 2005), we proposed a new version of the model which assumes a top-heavy IMF in starbursts (with slope $x = 0$, compared to Salpeter slope $x = 1.35$), but a normal solar neighbourhood IMF for quiescent star formation. In this new model, the star formation parameters were also changed to force more star formation to happen in bursts. This revised model agreed well with both the number counts and redshift distributions of SMGs detected at $850\mu\text{m}$, and with the rest-frame far-UV luminosity function of LBGs at $z \sim 3$, while still maintaining consistency with galaxy properties in the local Universe such as the optical, near-IR and far-IR luminosity functions, and gas fractions, metallicities, morphologies and sizes. In the third paper (Lacey et al. 2008), we compared predictions from the same Baugh et al. (2005) model (without changing any parameters) with observational data on galaxy evolution in the mid-IR from *Spitzer* and found generally good agreement.

This same model was found by Le Delliou et al. (2005, 2006) and Orsi et al. (2008) to provide a good match to the observed evolution of the population of Ly α -emitting galaxies, and of their clustering, over the redshift range $z \sim 3 - 6$. Support for the controversial assumption of a top-heavy IMF in bursts came from the studies of chemical enrichment in this model by Nagashima et al. (2005a,b), who found that the metallicities of both the intergalactic gas in galaxy clusters and the stars in elliptical galaxies were predicted to be significantly lower than observed values if a normal IMF was assumed for all star formation, but agreed much better if a top-heavy IMF in bursts was assumed, as in Baugh et al..

We also mention here an alternative semi-analytical approach using the GRASIL SED model which has been developed by Granato et al. (2004) and Silva et al. (2005). This approach differs

from that in the present paper, in that the treatment of mass assembly of galaxies is greatly simplified, neglecting halo and galaxy mergers, and modelling the disk population phenomenologically, but it does include a detailed treatment of the relation between QSO and spheroid formation, including feedback from the QSO phase on galaxy formation. Predictions for *Herschel* from this model have been presented in Negrello et al. (2007).

The outline of this paper is as follows: In §2, we review the physical ingredients in our model and the motivations for some of the key parameter choices. In §3 and §4, we present model predictions for the evolution of the galaxy luminosity function in the *Herschel* bands, and for the consequent number counts and redshift distributions. Next, in §5, we show predictions for some other key physical properties of *Herschel*-selected galaxies, while in §6, we show predictions for fluxes at other wavelengths from the far-UV to the radio. In §7 we try to answer the key cosmological question: what fraction of the dust-obscured star formation over the history of the Universe should the planned surveys with *Herschel* be able to uncover? In §8, we briefly discuss what the model predicts for clustering of galaxies in the *Herschel* bands. Finally, we present our conclusions in §9.

2 MODEL

The model used for the predictions in this paper is identical to that described in Baugh et al. (2005) and Lacey et al. (2008) (apart from minor code updates), so we give only a very brief summary here. We use the GALFORM semi-analytical galaxy formation model to predict the physical properties of the galaxy population at different redshifts, and combine it with the GRASIL spectrophotometric model to predict the detailed SEDs of model galaxies (including emission from dust).

2.1 GALFORM galaxy formation model

We compute the formation and evolution of galaxies within the framework of the Λ CDM model of structure formation using the semi-analytical galaxy formation model GALFORM. The general methodology and approximations behind the GALFORM model are set out in detail in Cole et al. (2000) (see also the review by Baugh 2006). In summary, the GALFORM model follows the main processes which shape the formation and evolution of galaxies. These include: (i) the collapse and merging of dark matter halos; (ii) the shock-heating and radiative cooling of gas inside dark halos, leading to the formation of galaxy disks; (iii) quiescent star formation in galaxy disks; (iv) feedback both from supernova explosions and from photo-ionization of the IGM; (v) chemical enrichment of the stars and gas; (vi) galaxy mergers driven by dynamical friction within common dark matter halos, leading to the formation of stellar spheroids, and also triggering bursts of star formation. The end product of the calculations is a prediction of the numbers and properties of galaxies that reside within dark matter haloes of different masses. The model predicts the stellar and cold gas masses of the galaxies, along with their star formation and merger histories, their disk and bulge sizes, and their metallicities.

The prescriptions and parameters for the different processes which we use in this paper are identical to those adopted by Baugh et al. (2005) and Lacey et al. (2008). The background cosmology is a spatially flat CDM universe with a cosmological constant, with ‘‘concordance’’ parameters $\Omega_m = 0.3$, $\Omega_\Lambda = 0.7$,

$\Omega_b = 0.04$, and $h \equiv H_0/(100\text{km s}^{-1}\text{Mpc}^{-1}) = 0.7$. The amplitude of the initial spectrum of density fluctuations is set by the r.m.s. linear fluctuation in a sphere of radius $8h^{-1}\text{Mpc}$, $\sigma_8 = 0.93$. The assembly and merger histories of dark matter halos are computed using a Monte Carlo method based on the extended Press-Schechter model (Cole et al. 2000). When used in galaxy formation models, these Monte Carlo merger histories have been found to give very similar results to using halo merger histories extracted directly from N-body simulations (e.g. Helly et al. 2003). The evolution of the baryons within the dark halos is then calculated using analytical prescriptions for gas cooling, star formation, supernova feedback etc. The parameters of the GALFORM model describing these baryonic processes were chosen to reproduce a range of properties of present-day galaxies (optical, near-IR and far-IR luminosity functions, fraction of spheroid- vs disk-dominated galaxies, and galaxy disk sizes, gas fractions and metallicities as a function of luminosity), as well as the number counts and redshift distribution of sub-mm galaxies, and the rest-frame far-UV luminosity function of Lyman-break galaxies at high redshift (Baugh et al. 2005).

An important feature of our model is the existence of two modes of star formation, the “quiescent” mode in galaxy disks, and the “burst” mode triggered by galaxy mergers. In the current model, starbursts are triggered by both major galaxy mergers (which transform stellar disks to spheroids) and minor galaxy mergers (which leave the stellar disk of the larger galaxy unchanged). The two modes of star formation are assumed to have different stellar Initial Mass Functions (IMFs). Both IMFs are taken to be piecewise power laws, with slopes x defined by $dN/d \ln m \propto m^{-x}$, where N is the number of stars and m is the stellar mass (so the Salpeter slope is $x = 1.35$), and covering a stellar mass range $0.15 < m < 120M_\odot$. Quiescent star formation in galaxy disks is assumed to have a solar neighbourhood IMF, for which we use the Kennicutt (1983) parametrization, with slope $x = 0.4$ for $m < M_\odot$ and $x = 1.5$ for $m > M_\odot$. (The Kennicutt (1983) IMF is similar to other popular parametrizations of the solar neighbourhood IMF, such as that of Kroupa (2001).) Bursts of star formation triggered by galaxy mergers are assumed to form stars with a top-heavy IMF with slope $x = 0$. The different IMFs result in different luminosities and SEDs for a stellar population, as well as different overall rates of gas return and metal ejection from dying stars. These effects are all taken into account self-consistently, based on the predictions from stellar evolution models.

As discussed in detail in Baugh et al. (2005), the top-heavy IMF in bursts was found to be required in order to reproduce the observed number counts and redshift distributions of the faint sub-mm galaxies. The top-heavy IMF results both in higher bolometric luminosities for young stellar populations, and greater production of heavy elements and hence also dust, both effects being important for reproducing the properties of SMGs in the model. Furthermore, as shown by Nagashima et al. (2005a,b), the predicted chemical abundances of the X-ray emitting gas in galaxy clusters and of the stars in elliptical galaxies also agree better with observational data in a model with the top-heavy IMF in bursts, rather than a universal solar neighbourhood IMF. Subsequent work using the same model has also shown that it predicts galaxy evolution in the mid-IR in good agreement with observations by *Spitzer* (Lacey et al. 2008). A more detailed comparison of the model with the properties of observed SMGs has been carried out by Swinbank et al. (2008). As shown by Le Delliou et al. (2005, 2006) and Orsi et al. (2008), the same model also reproduces the observed evolution of the luminosity function and clustering of Ly α emitting galaxies at high redshift. Finally, González et al. (2009) have made a detailed comparison of

the model with the luminosity function, colours, morphologies and sizes of galaxies in the SDSS survey of the local Universe.

A variety of other observational evidence has accumulated which suggests that the IMF in some environments may be top-heavy compared to the solar neighbourhood IMF (see Elmegreen (2009) for a recent review). Rieke et al. (1993) argued for a top-heavy IMF in the nearby starburst M82, based on modelling its integrated properties, while Parra et al. (2007) found possible evidence for a top-heavy IMF in the ultra-luminous starburst Arp220 from the relative numbers of supernovae of different types observed at radio wavelengths. Evidence has been found for a top-heavy IMF in some star clusters in intensely star-forming regions, both in M82 (e.g. McCrady et al. 2003), and in our own Galaxy (e.g. Figer et al. 1999; Stolte et al. 2005; Harayama et al. 2008). Observations of both the old and young stellar populations in the central 1 pc of our Galaxy also favour a top-heavy IMF (Paumard et al. 2006; Maness et al. 2007). In the local Universe, Meurer et al. (2009) find evidence for variations in the IMF between galaxies from variations in the H α /UV luminosity ratio. Fardal et al. (2007) found that reconciling measurements of the optical and IR extragalactic background with measurements of the cosmic star formation history also seemed to require an average IMF that was somewhat top-heavy. Pérez-González et al. (2008) compared observational constraints on the evolution of the star formation rate density and stellar mass density over cosmic time, and found that reconciling these two types of data also favours a more top-heavy IMF at higher redshifts, as had been hinted at by earlier studies. Finally, van Dokkum (2008) found that reconciling the colour and luminosity evolution of early-type galaxies in clusters also favoured a top-heavy IMF. Larson (1998) summarized other evidence for a top-heavy IMF during the earlier phases of galaxy evolution, and argued that this could be a natural consequence of the temperature-dependence of the Jeans mass for gravitational instability in gas clouds. Larson (2005) extended this to argue that a top-heavy IMF might also be expected in starburst regions, where there is strong heating of the dust by the young stars.

In our model, the fraction of star formation occurring in the burst mode increases with redshift (see Baugh et al. 2005), so the average IMF with which stars are being formed shifts from being close to a solar neighbourhood IMF at the present day to being very top-heavy at high redshift. In this model, 30% of star formation occurred in the burst mode when integrated over the past history of the Universe, but only 6% of the current stellar mass was formed in bursts, because of the much larger fraction of mass recycled by dying stars for the top-heavy IMF. We note that our predictions for the IR and sub-mm luminosities of starbursts are not sensitive to the precise form of the top-heavy IMF, but simply require a larger fraction of $m \sim 5 - 20M_\odot$ stars relative to a solar neighbourhood IMF.

We note that the galaxy formation model in this paper, unlike some other recent semi-analytical models, does not include AGN feedback. Instead, the role of AGN feedback in reducing the amount of gas cooling to form massive galaxies is taken by superwinds driven by supernova explosions. These superwinds eject gas from galaxy halos, reducing the mass of hot gas and hence also the rate of gas cooling in halos. The first semi-analytical model to include AGN feedback was that of Granato et al. (2004), who introduced a detailed model of feedback from QSO winds during the formation phase of supermassive black holes (SMBHs), with the aim of explaining the co-evolution of the spheroidal components of galaxies and their SMBHs. The predictions of the Granato et al. model for number counts and redshift distributions in the IR have

been computed by Silva et al. (2005) using the GRASIL spectrophotometric model, and compared to *ISO* and *Spitzer* data. However, the Granato et al. (2004) model has the limitations that it does not include the merging of galaxies or of dark halos, and does not treat the formation and evolution of galactic disks. More recently, several semi-analytical models have been published which propose that heating of halo gas by relativistic jets from an AGN in an optically inconspicuous or “radio” mode can balance radiative cooling of gas in high-mass halos, thus suppressing *hot accretion* of gas onto galaxies (Bower et al. 2006; Croton et al. 2006; Cattaneo et al. 2006; Monaco et al. 2007; Lagos et al. 2008). However, these AGN feedback models differ in detail, and all are fairly schematic. None of these models has been shown to reproduce both the observed number counts and the observed redshifts of the faint sub-mm galaxies.

The effects of our superwind feedback are qualitatively quite similar to those of the radio-mode AGN feedback. Both superwind and AGN feedback models contain free parameters, which are adjusted in order to make the model fit the bright end of the observed present-day galaxy luminosity function at optical and near-IR wavelengths. However, since the physical mechanisms are different, they make different predictions for how the galaxy luminosity function should evolve with redshift. Current models for the radio-mode AGN feedback are very schematic, but they have the advantage over the superwind model that the energetic constraints are greatly relaxed, since accretion onto black holes can convert mass into energy with a much higher efficiency than can supernova explosions. We will investigate the predictions of models with AGN feedback for the IR and sub-mm evolution of galaxies in a future paper.

2.2 GRASIL model for stellar and dust emission

For each galaxy in our model, we compute the spectral energy distribution using the spectrophotometric model GRASIL (Silva et al. 1998; Granato et al. 2000). GRASIL computes the emission from the stellar population, the absorption and emission of radiation by dust, and also radio emission (thermal and synchrotron) powered by massive stars (Bressan et al. 2002).

The main features of the GRASIL model are as follows:

- (i) The stars are assumed to have an axisymmetric distribution in a disk and a bulge.
- (ii) The SEDs of the stellar populations are calculated separately for the disk and the bulge, according to the distribution of stars in age and metallicity that is obtained from the corresponding star formation and chemical enrichment histories. We use the population synthesis model described in Bressan et al. (1998), which is based on the Padova stellar evolution tracks and Kurucz model atmospheres. This model is able to reproduce fairly well the integrated UV properties of Globular Clusters (Chavez et al. 2009) and the observed *Spitzer* IRS spectra and mid-IR colours of ellipticals in the Virgo and Coma clusters (Bressan et al. 2006; Clemens et al. 2009), i.e. old stellar populations likely at the two extremes of the metallicity range of stellar systems. At intermediate and young ages, it compares well with recent observations of LMC star clusters (see e.g. Mollá et al. 2009)
- (iii) The cold gas and dust in a galaxy are assumed to be in a 2-phase medium, consisting of dense gas in giant molecular clouds embedded in a lower-density diffuse component. In a quiescent galaxy, the dust and gas are assumed to be confined to the disk, while for a galaxy undergoing a burst, the dust and gas are confined to the spheroidal burst component.

(iv) Stars are assumed to be born inside molecular clouds, and then to leak out into the diffuse medium on a timescale t_{esc} . As a result, the youngest and most massive stars are concentrated in the dustiest regions, so they experience larger dust extinctions than older, typically lower-mass stars, and dust in the clouds is also much more strongly heated than dust in the diffuse medium.

(v) The extinction of the starlight by dust is computed using a radiative transfer code; this is used also to compute the intensity of the stellar radiation field heating the dust at each point in a galaxy.

(vi) The dust is modelled as a mixture of graphite and silicate grains with a continuous distribution of grain sizes (varying between 8\AA and $0.25\ \mu\text{m}$), and also Polycyclic Aromatic Hydrocarbon (PAH) molecules with a distribution of sizes. The equilibrium temperature in the local interstellar radiation field is calculated for each type and size of grain, at each point in the galaxy, and this information is then used to calculate the emission from each grain. In the case of very small grains and PAH molecules, temperature fluctuations are important, and the probability distribution of the temperature is calculated. The detailed spectrum of the PAH emission is obtained using the PAH cross-sections from Li & Draine (2001), as described in Vega et al. (2005). The grain size distribution is chosen to match the mean dust extinction curve and emissivity in the local ISM, and is not varied, except that the PAH abundance in molecular clouds is assumed to be 10^{-3} of that in the diffuse medium (Vega et al. 2005).

(vii) Radio emission from ionized gas in HII regions and synchrotron radiation from relativistic electrons accelerated in supernova remnant shocks are calculated as described in Bressan et al. (2002).

The output from GRASIL is then the complete SED of a galaxy from the far-UV to the radio (wavelengths $100\text{\AA} \lesssim \lambda \lesssim 1\text{m}$). The SED of the dust emission is computed as a sum over the different types of grains, having different temperatures depending on their size and their position in the galaxy. The dust SED is thus intrinsically multi-temperature. GRASIL has been shown to give an excellent match to the observed SEDs of galaxies of all types, from passive systems through to ULIRGs (Silva et al. 1998; Vega et al. 2008). We show some example SEDs from the combined GALFORM + GRASIL code in Fig. 1.

3 EVOLUTION OF THE GALAXY LUMINOSITY FUNCTION IN THE FAR-IR

We begin by showing what the model predicts for the evolution of the galaxy luminosity function (LF) at the far-IR wavelengths which will be probed by *Herschel*, before moving on to predictions for more immediately observable quantities in the next section. Fig. 2 shows how the predicted luminosity function evolves from $z = 0$ to $z = 6$. The top-left panel shows the LF of the total mid+far-IR luminosity L_{IR} , defined as the integral over the galaxy SED from 8 to $1000\ \mu\text{m}$. This range includes almost all of the dust emission from a galaxy, but hardly any of the stellar emission. The total IR LF evolves strongly with redshift, increasing in characteristic luminosity and number density from $z = 0$ to $z \sim 2$, having a plateau from $z \sim 2$ to $z \sim 4$, and then gradually declining at higher redshifts. This evolution results from the combined effects of the evolution of the galaxy SFR distribution and the shift in the dominant mode of star formation from quiescent (with a normal IMF) at low redshift to burst (with top-heavy IMF) at higher redshift. - this is discussed further in §7. Starting from very high redshift, the cosmic star formation density increases to a peak at

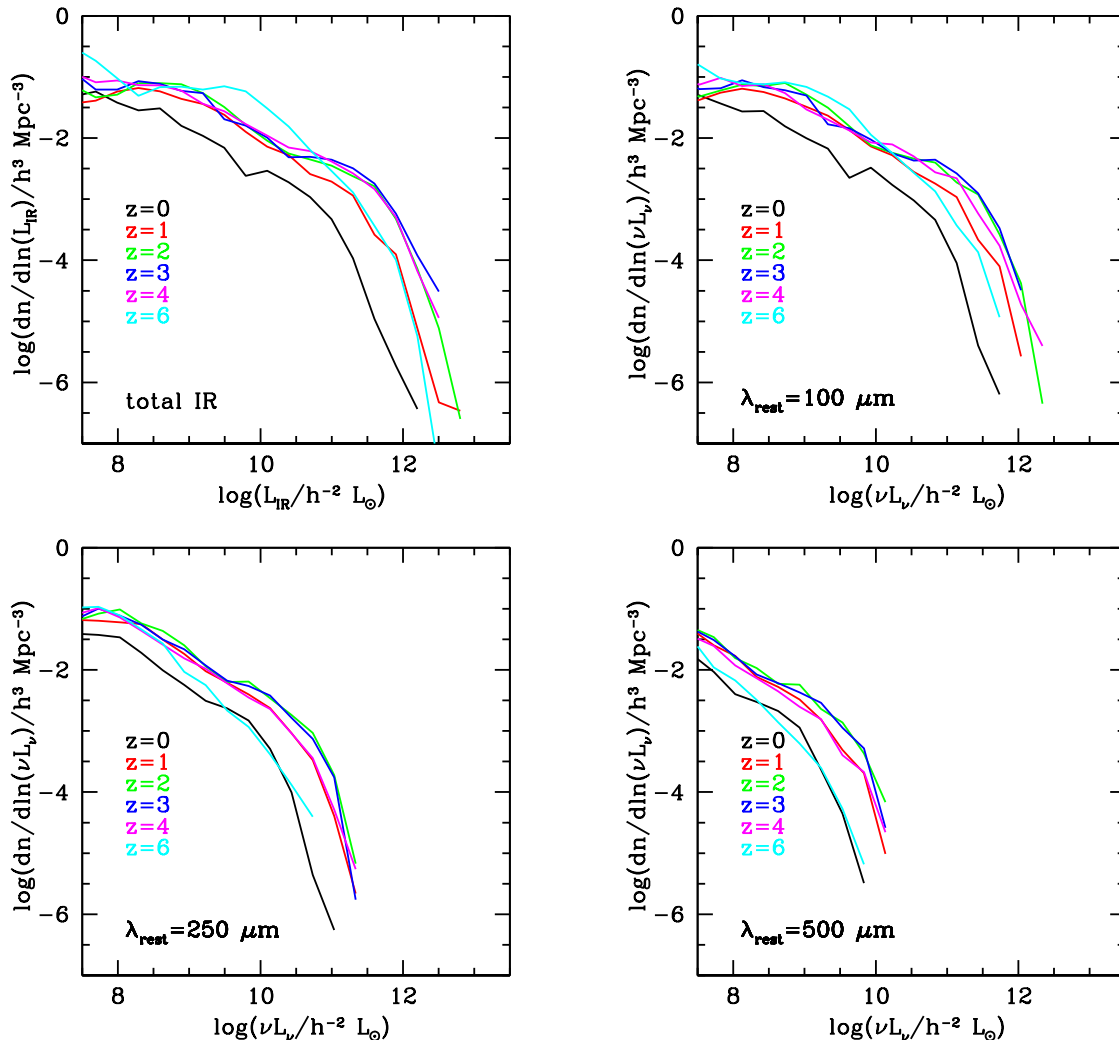


Figure 2. Predicted evolution of the galaxy LF in the far-IR. The LFs are shown at redshifts $z = 0, 1, 2, 3, 4, 6$, with different redshifts shown by different colours, as indicated by the key. (a) Total IR (8-1000 μm) luminosity. (b) Rest-frame 100 μm . (c) Rest-frame 250 μm . (d) Rest-frame 500 μm .

$z \sim 2 - 3$, driven by the build-up of dark matter halos in which gas is able to cool and form stars, and then declines down to $z = 0$, driven by the declining efficiency of gas cooling in halos as their masses become even larger. Over the redshift range $z \sim 0 - 3$, the characteristic luminosity increases by a factor ~ 8 , while the number density of LIRGs (Luminous Infrared Galaxies, defined to have $L_{IR} = 10^{11} L_{\odot}$) increases by a factor ~ 10 , and the number density of ULIRGs (Ultra-luminous Infrared Galaxies, defined to have $L_{IR} = 10^{12} L_{\odot}$) increases by a factor ~ 300 . The other panels in Fig. 2 show the predicted evolution of the LF at rest-frame wavelengths of 100, 250 and 500 μm (calculated through the PACS and SPIRE bandpasses). The evolution of the LF at these wavelengths is qualitatively similar to that of the total IR LF. The 100 μm LF looks very similar to the total IR LF, both in the form of the evolution and in normalization (when νL_{ν} is used as the luminosity variable), reflecting the fact that the far-IR SEDs peak around this wavelength. At longer wavelengths, the characteristic luminosity is fainter (in terms of νL_{ν}), reflecting the decline in the SED longwards of the peak; the degree of evolution is also somewhat less (a factor ~ 5 in characteristic luminosity at 500 μm over the redshift

range $z \sim 0 - 3$), reflecting a shift in the average far-IR SED shape to somewhat warmer dust temperatures at higher redshifts.

4 NUMBER COUNTS AND REDSHIFT DISTRIBUTIONS

4.1 Number counts

We now move on to make predictions for the quantities which can be measured most directly in cosmological galaxy surveys with *Herschel*. The planned cosmological surveys will concentrate on imaging in the three PACS bands (centred at 70, 100 and 160 μm) and the three SPIRE bands (centred at 250, 350 and 500 μm); *Herschel* spectroscopy will be limited to fewer and brighter sources. The simplest observable quantity is the number counts per solid angle of galaxies as a function of flux, S_{ν} , which we plot in the form $dN/d\ln S_{\nu}$.

An observational estimate of the number counts in the SPIRE bands has already been made using the BLAST balloon-borne telescope (Devlin et al. 2009; Patanchon et al. 2009), so we first compare our model predictions with those data in Fig. 3. The BLAST results are for a single 9 deg² field. The BLAST maps have

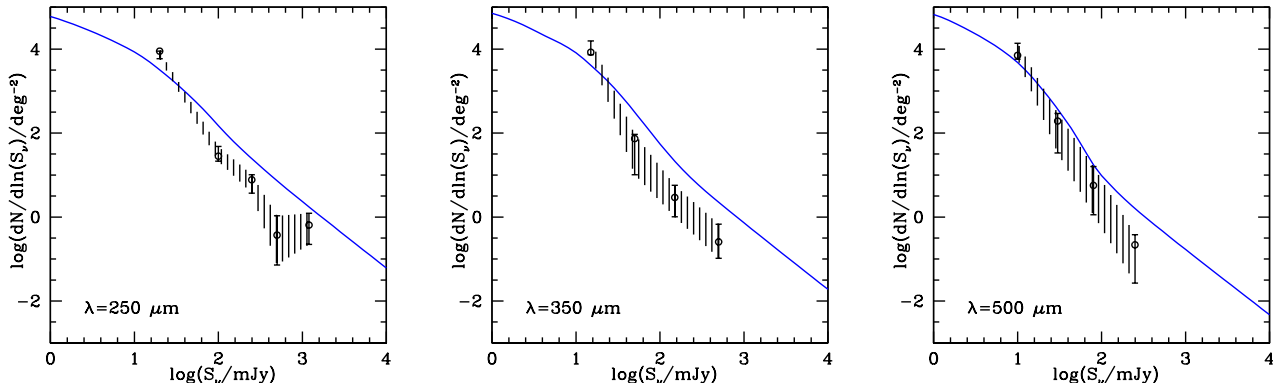


Figure 3. Predicted galaxy differential number counts in the SPIRE bands (blue curves) compared to observational estimates from BLAST (Patanchon et al. 2009), shown in black. The observational estimates were obtained by modelling the $P(D)$ distribution, rather than identifying individual sources. The points show the “best estimates”, while the error bars and shaded regions show the 68% confidence ranges.

two times worse angular resolution than *Herschel* and are also quite noisy, which leads to serious problems with confusion, incompleteness and Eddington bias. As discussed by the BLAST authors, this means that a direct determination of the counts by identifying individual sources is not feasible. They therefore estimated the counts using a “ $P(D)$ ” analysis, fitting a piecewise power-law model to the distribution of pixel brightnesses in the maps at each wavelength. The results of this are shown in the figure, with the points showing the best estimate of the counts at each of the nodes of the model fit, and the error bars and shaded region showing the 68% confidence region. Note that the BLAST $P(D)$ analysis assumed that the sources were not clustered. Including clustering could both change the best estimate values, and increase the error bars on the estimated counts. We see that the predicted counts agree well with the BLAST estimates at faint fluxes, but are a little higher at bright fluxes, especially at the shorter wavelengths. However, given the aforementioned uncertainties in the BLAST results, and the limited sky coverage, these differences should not be taken as conclusive at this stage, and a definitive test must await the results from *Herschel*.

Next, in Fig. 4 we show the predicted differential number counts in the PACS and SPIRE imaging bands, for the full range of fluxes and wavelengths covered by *Herschel*, with each panel corresponding to a different wavelength. In each panel, the blue curve shows the predicted total counts, while the green and red curves show the separate contributions to these from quiescent galaxies and ongoing bursts. (A note about our terminology: by “bursts” we mean any galaxy with ongoing star formation in the burst mode, while by “quiescent” we mean all other galaxies, whether undergoing star formation only in the disk mode, or completely passive with no current star formation. However, completely passive systems contribute very little to the luminosity functions and number counts at far-IR wavelengths.) We see that quiescent galaxies dominate the counts at brighter fluxes in all bands, while the bursts tend to dominate at faint fluxes, reflecting the increasing domination of the starburst mode of star formation at higher redshifts.

We can use our model to predict the flux levels at which sources should become confused in the different *Herschel* bands. Source confusion happens when multiple sources are separated in angle by less than the angular resolution of the telescope, and so appear merged together in images. Since the number of sources increases with decreasing flux, confusion sets a lower limit to the flux

λ [μm]	θ_{FWHM} [arcsec]	S_{conf} [mJy]	γ_{conf}	z_{50}	z_{90}
70	5.2	0.24	0.88	1.15	2.53
100	7.7	1.6	0.95	0.80	1.76
160	12	9.5	1.28	0.72	1.57
250	19	22	1.78	0.70	1.64
350	24	21	2.17	0.93	1.93
500	35	19	2.58	1.21	1.93

Table 1. Predicted confusion limits for *Herschel* imaging. λ is the wavelength, θ_{FWHM} is the angular resolution of PACS or SPIRE imaging at that wavelength, S_{conf} is the predicted flux at the confusion limit, and γ_{conf} is the slope of the differential source counts at that flux. z_{50} and z_{90} are the predicted median and 90-percentile redshifts for galaxies brighter than S_{conf} .

at which one can still identify separate sources in an image (regardless of the integration time used). Confusion will be a serious problem in deep cosmological surveys with *Herschel* due to the relatively poor angular resolution of the telescope (compared to optical telescopes). This confusion limit depends both on the angular resolution of the telescope and on the actual surface density of sources per solid angle as a function of flux. We estimate the confusion limit using the *source density criterion* (Condon 1974; Väisänen et al. 2001): if the telescope has a FWHM (full width at half maximum) beamwidth of θ_{FWHM} , we define the effective beam solid angle as $\omega_{beam} = (\pi/(4 \ln 2)) \theta_{FWHM}^2 = 1.13 \theta_{FWHM}^2$, and then define the confusion limited flux S_{conf} to be such that $N(> S_{conf}) = 1/(\mathcal{N}_{beam} \omega_{beam})$, where $N(> S)$ is the number per solid angle of sources brighter than flux S . This estimate ignores any clustering of the sources. We choose $\mathcal{N}_{beam} = 20$ for the number of beams per source at the confusion limit, which gives similar results to more detailed analyses (Väisänen et al. 2001; Dole et al. 2004). We have calculated confusion limits in the different *Herschel* bands using our predicted number counts, together with the assumed beamsizes given in Table 1. The predicted confusion limited fluxes are given in the table and plotted as vertical black dashed lines in Fig. 4. Since *Herschel* images will be essentially diffraction-limited, confusion sets in at a lower source density at longer wavelengths, which typically implies a brighter flux.

We also indicate in Fig. 4 by vertical and horizontal dashed

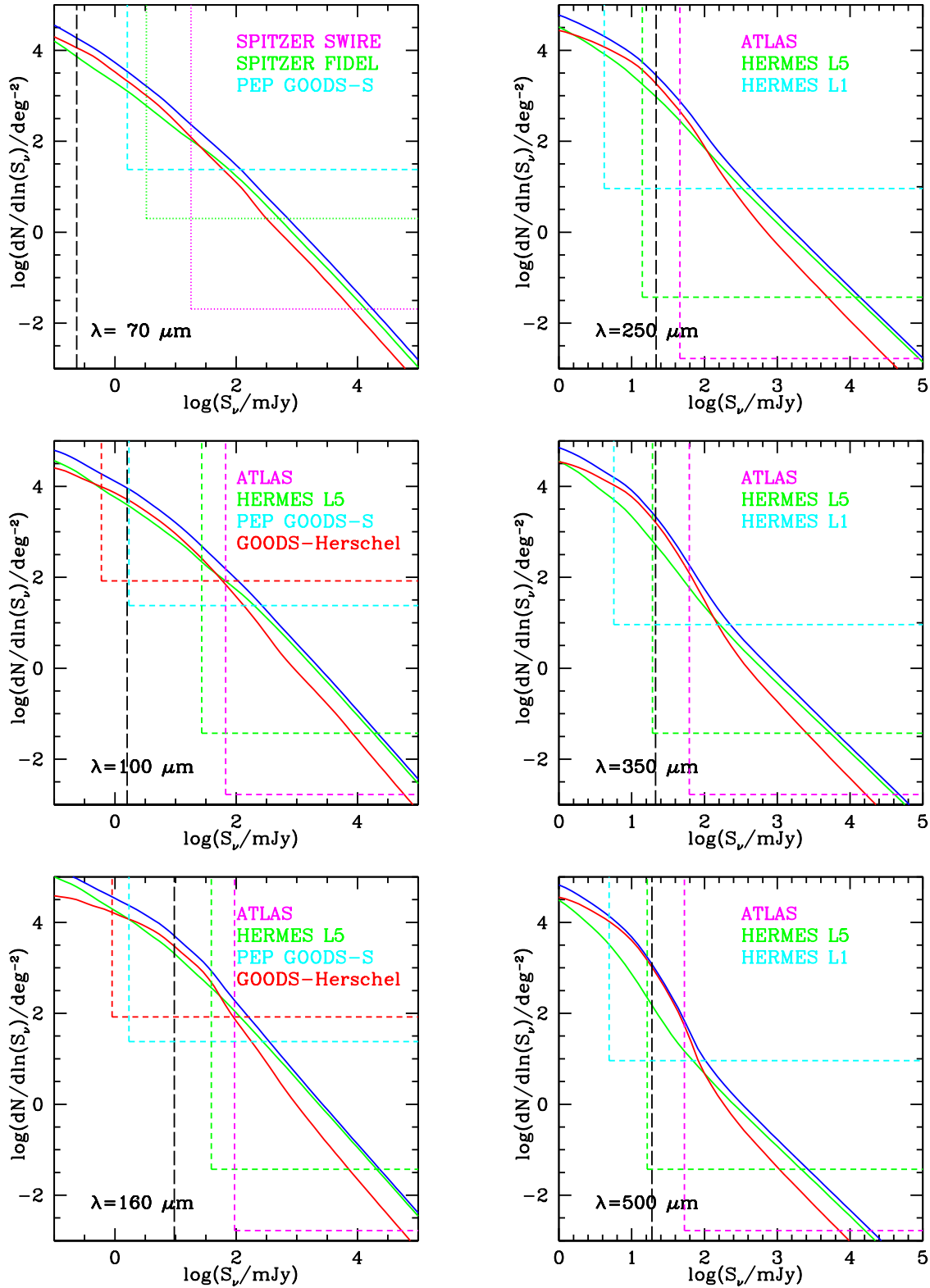


Figure 4. Galaxy differential number counts in the six *Herschel* bands. We show three different curves for our standard model - solid blue: total counts including dust extinction and emission; solid red: ongoing bursts; solid green: quiescent galaxies. The vertical dashed black lines show the estimated confusion limit for the model at each wavelength, calculated as described in §4.1. The vertical and horizontal dashed coloured lines show the flux and area limits for some planned Key Project surveys, as indicated in the key.

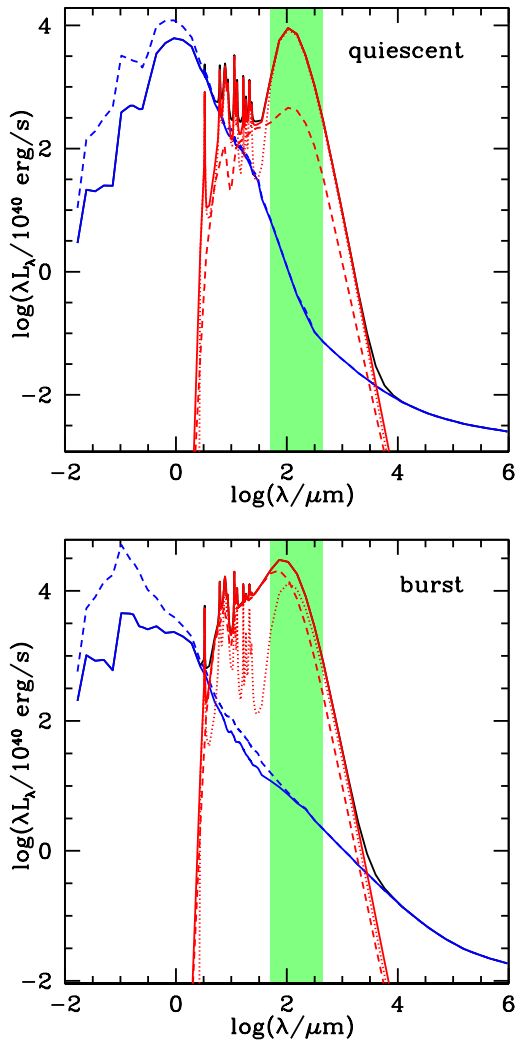


Figure 1. Example SEDs from GALFORM+ GRASIL. (a) Quiescently star-forming disk galaxy at $z = 0$. (b) Starburst at $z = 0$ seen one e-folding time after start of burst. The blue lines show the “stellar” emission (which includes emission from dust in AGB star envelopes, and thermal and synchrotron radio emission from the ISM), both with (solid lines) and without (dashed lines) dust extinction. The red lines show emission from interstellar dust, both the total (solid line) and the separate contributions from molecular clouds (dashed line) and the diffuse ISM (dotted line). The shaded green region shows the wavelength range $60\text{--}600\mu\text{m}$ covered by the *Herschel* imaging bands.

coloured lines the regions of flux and surface density that are planned to be probed by the main cosmological galaxy surveys with *Herschel*. For each survey, the vertical line indicates the nominal flux limit S_{min} set by integration time and signal-to-noise (ignoring possible source confusion), and the horizontal line indicates the minimum surface density of sources that can be probed given the solid angle A of the survey, which we estimate as $(dN/d\ln S)_{min} = 1/A$. We consider here the following four planned surveys, which are all *Herschel* Key Programmes¹. The first three are deep surveys, while the last is a shallower wide-area survey. The deep surveys have various tiers, but for simplicity we

here consider only the deepest blank-field tier in each survey, since this sets the limit for how far down in luminosity the survey can probe at each redshift, except for HERMES, where we also consider a shallower tier.

*GOODS-Herschel*²:

This survey using PACS and SPIRE will have 2 tiers, “ultradeep” and “superdeep”, and will include the deepest imaging in the PACS 100 and $160\mu\text{m}$ bands of any of the cosmological key programmes. We consider here the ultradeep tier, which is in the GOODS-S field.

*PACS Evolutionary Probe (PEP)*³:

This deep imaging survey using PACS, which is coordinated with the HERMES survey, will include blank fields covering a range of 4 in limiting flux and 50 in area, mainly in the 100 and $160\mu\text{m}$ bands. We consider here the deepest blank field, which is the GOODS-S field.

*Herschel Multi-tiered Extragalactic Survey (HERMES)*⁴:

This survey, using both PACS and SPIRE, and coordinated with PEP, will be the largest of the cosmological surveys in terms of observing time. It will include 6 tiers of blank field surveys, covering a range of 6 in limiting flux and 400 in area. We consider here the deepest tier, Level-1 (the CDFS/GOODS-S field), and also a shallower tier, Level-5 (the XMM, ELAIS-N1-SCUBA, Bootes-SCUBA2, EGS-SCUBA2, CDFS and Lockman fields), which is intermediate in area and in depth in the SPIRE bands between Level-1 and the shallower ATLAS survey.

*Herschel ATLAS*⁵:

This survey, using PACS and SPIRE, will be the shallowest of the cosmological surveys, but will cover by far the largest area. There is only a single tier.

Table 2 lists the basic parameters (wavelengths, areas and flux limits ignoring confusion) for these planned surveys (or tiers within surveys) which we will show in subsequent figures. These surveys are plotted in Fig. 4. These survey parameters may be modified once the inflight performance of the telescope is known.

It can be seen from Fig. 4 that, taken together, the *Herschel* surveys at each wavelength (excepting $70\mu\text{m}$) should contain galaxies covering a huge range ($\sim 10^4 - 10^5$) in flux. At $70\mu\text{m}$, the planned *Herschel* surveys probe only slightly deeper than surveys already carried out using *Spitzer*. We show in the panel the regions of flux and source density probed by two of these *Spitzer* surveys, SWIRE⁶ ($A = 49 \text{ deg}^2$, $S_{min} = 18 \text{ mJy}$ Lonsdale et al. 2003) and FIDEL⁷ ($A = 0.5 \text{ deg}^2$, $S_{min} = 3.3 \text{ mJy}$, Dickinson & FIDEL team 2007; Huynh et al. 2007). The *Herschel* PEP GOODS-S survey will probe about two times fainter than *Spitzer* but still well above the predicted *Herschel* confusion limit. At $100\mu\text{m}$, the PEP survey is predicted to be at the confusion limit, while the GOODS-HERSCHEL survey will be below it. Confusion is predicted to be worst in the $160\mu\text{m}$ deep surveys, where the sensitivity of the GOODS-HERSCHEL survey will be 10 times below the predicted confusion limit, and that for PEP GOODS-S 6 times below it. At the longer SPIRE wavelengths (250, 350 and $500\mu\text{m}$), the deepest blank field tier (L1) of the HERMES survey will be 4–5 times fainter than the predicted confusion limit, while L5 tier will be at or slightly below confusion. The ATLAS survey

² <http://herschel.esac.esa.int/Docs/KPOT>

³ <http://www.mpe.mpg.de/ir/Research/PEP>

⁴ <http://astronomy.sussex.ac.uk/~sjo/Hermes>

⁵ <http://herschel.esac.esa.int/Docs/KPOT>

⁶ <http://swire.ipac.caltech.edu/swire>

⁷ <http://irsa.ipac.caltech.edu/data/SPITZER/FIDEL>

¹ http://herschel.esac.esa.int/Key_Programmes.shtml

Survey	A [deg ²]	λ [μm]	S_{min} [mJy]	N_{gal}	z_{50}	z_{90}
GOODS-Herschel	0.012	100	0.6	270	0.99	2.22
Ultra-deep		160	0.9	540	1.17	2.57
PEP GOODS-S	0.042	70	1.6	130	0.64	1.51
		100	1.7	380	0.79	1.73
		160	1.7	1.1×10^3	1.09	2.28
HERMES Level-1	0.11	250	4.2	1.9×10^3	1.25	2.42
		350	5.7	1.2×10^3	1.42	2.61
		500	4.9	930	1.66	2.98
HERMES Level-5	27	100	27	1.0×10^4	0.32	0.78
		160	39	1.4×10^4	0.37	0.96
		250	14	9.0×10^4	0.88	1.86
		350	19	3.4×10^4	0.97	1.99
		500	16	1.9×10^4	1.26	2.08
ATLAS	600	100	67	6.9×10^4	0.21	0.50
		160	94	7.3×10^4	0.21	0.50
		250	46	2.2×10^5	0.41	1.28
		350	62	4.6×10^4	0.27	1.33
		500	53	1.4×10^4	0.20	1.22

Table 2. Basic parameters for the surveys (or tiers within surveys) being modelled. The area A is the total value for that tier, and may include multiple fields. Limiting fluxes S_{min} are 5σ and ignore confusion. For HERMES Level-5 some of the flux limits vary between different fields, so we give the values corresponding to the majority of the survey area. N_{gal} is the predicted total number of galaxies in that tier, and z_{50} and z_{90} are their predicted median and 90-percentile redshifts.

is predicted to be safely above the confusion limit (by factors of 2–40) at all wavelengths.

Various techniques will allow one to probe observationally sources fainter than the formal confusion limit, the principal ones being *pixel brightness distributions*, *gravitational lensing* and *multi-wavelength analysis*. In *pixel brightness distribution* (or $P(D)$) methods, one uses the distribution of pixel brightness to make statistical inferences about the slope and amplitude of the source counts at and below the confusion limit, without trying to identify the individual sources responsible (e.g. Patanchon et al. 2009). In *gravitational lensing*, one uses the gravitational magnification of the images of faint background galaxies by a foreground galaxy cluster to reduce confusion effects. Since both source fluxes and areas get multiplied by the magnification $\mathcal{A} > 1$, the cumulative source counts transform as $N(> S) = (1/\mathcal{A})N_0(> S/\mathcal{A})$, where $N_0(> S)$ is the unlensed distribution. If the source counts have the power-law form $dN/d\ln S \propto S^{-\gamma}$, then the intrinsic (unlensed) flux at the confusion limit is reduced by a factor $\mathcal{A}^{-1/\gamma}$ due to lensing. Table 1 lists the source count slopes predicted at the confusion limit for the different *Herschel* bands. It can be seen that the predicted slope γ_{conf} at the confusion limit increases with increasing wavelength, implying that gravitational lensing can potentially allow one to probe further below the *Herschel* confusion limits at shorter wavelengths. For example, for a gravitational magnification $\mathcal{A} = 10$, the effective confusion limit is lowered by factors of 0.09–0.4 as the wavelength increases from 100 to $500\mu\text{m}$. Finally, in *multi-wavelength analysis*, one combines images at different wavelengths having different angular resolutions. Variants of this include *multi-wavelength priors*, where one starts from a source list obtained from higher angular resolution data at some other wavelength, and tries to extract fluxes for individual confused sources at the target wavelength, and *multi-wavelength stacking*, where one tries to measure mean fluxes only (e.g. Dole et al. 2006; Marsden et al. 2009).

4.2 Redshift distributions

Having identified sources in images and measured their counts as a function of flux, the next key step observationally is to measure their redshifts (either spectroscopically or using photometric redshift methods), and construct redshift distributions in different flux ranges. We therefore consider the model predictions for redshift distributions next.

Firstly, in Fig. 5, we show the predicted median redshift (together with the 10% and 90% percentiles) as a function of flux in each of the PACS and SPIRE bands. As in Fig. 4, we also indicate the flux at the confusion limit and at the different Key Project survey limits by vertical dashed black and coloured lines respectively. The predicted median and 90% percentile redshifts for each survey tier are also given in Table 2. We see from the figure that the median redshifts for sources at the confusion limit are around $z_{50} \sim 1 - 1.5$, with the highest values at the shortest and longest *Herschel* wavelengths. If one assumes that the confusion limit can be completely circumvented, then of the surveys listed, HERMES-L1 at $500\mu\text{m}$ will probe to the highest median redshift ($z_{50} \approx 1.8$). If one assumes instead that confusion sets a hard limit, then the highest median redshift is reduced to $z_{50} \approx 1.4$, again achieved in the HERMES-L1 survey at $500\mu\text{m}$.

We now look at the redshift distributions in more detail. Fig. 6 shows the predicted redshift distributions for galaxies at the confusion limits listed in Table 1. In this figure, the redshift distributions have all been normalized to unit area under the curve to allow easier comparison of their shapes. We have included the redshift distribution at the $70\mu\text{m}$ confusion limit for completeness, even though none of the planned surveys at $70\mu\text{m}$ will go this faint. Apart from $500\mu\text{m}$, all of the redshift distributions peak at quite modest redshifts, $z \sim 0.4 - 0.8$, although there is a tail of objects to $z \sim 2$. The redshift peak gets broader with increasing wavelength, until at the longest wavelength, $500\mu\text{m}$, it splits into two peaks, with the main peak at $z \approx 1.4$ and a smaller peak at $z \approx 0.2$. This effect at $500\mu\text{m}$ is a manifestation of the *negative k-correction*, whereby

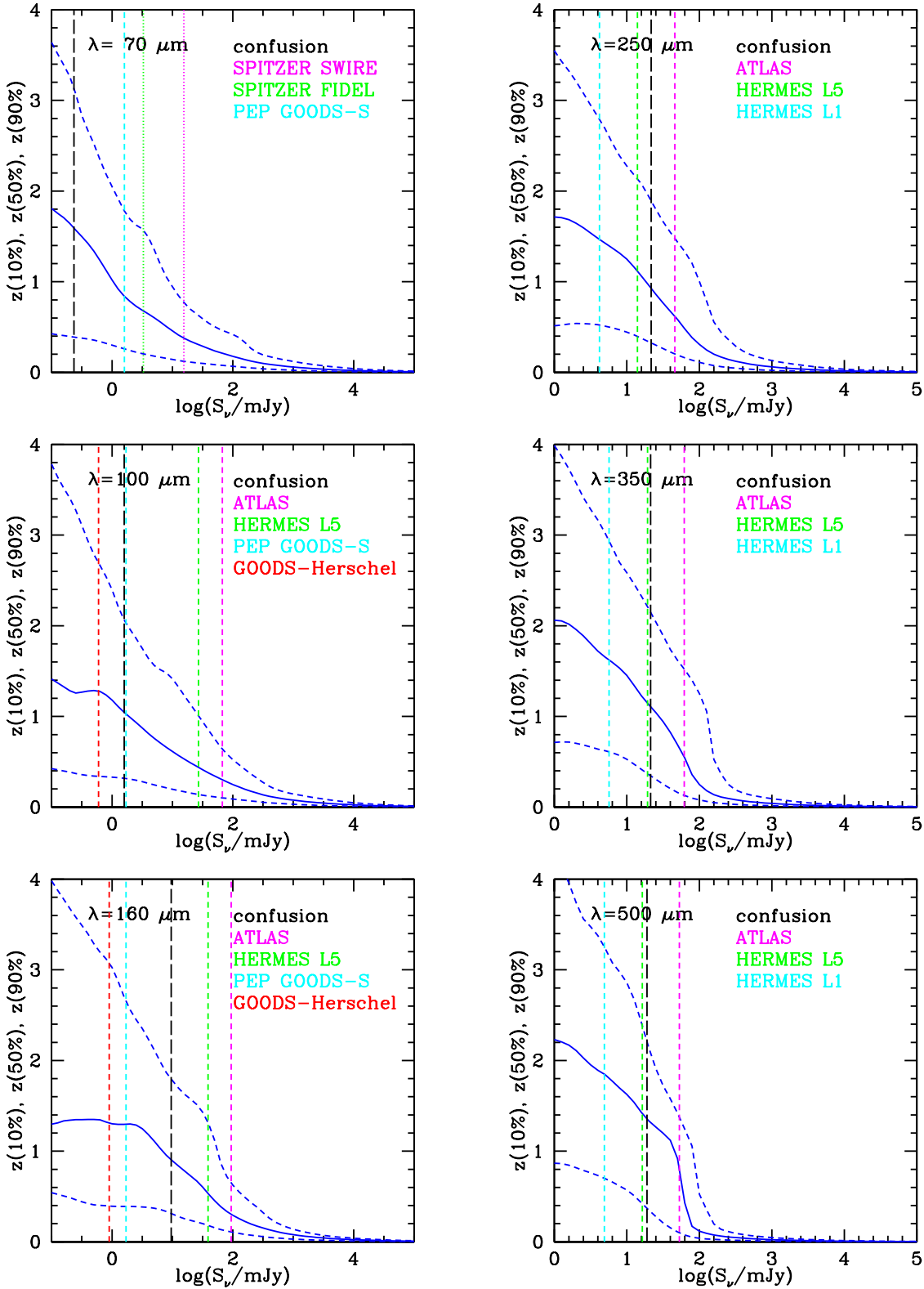


Figure 5. Median and percentiles of predicted redshift distributions as functions of flux in the six *Herschel* bands. The solid blue lines show the median and the dashed lines the 10% and 90% percentiles for galaxies at each flux. The vertical dashed black line shows the estimated confusion limit for the model at each wavelength. The coloured lines show the flux limits for some planned Key Project surveys, as indicated in the key.

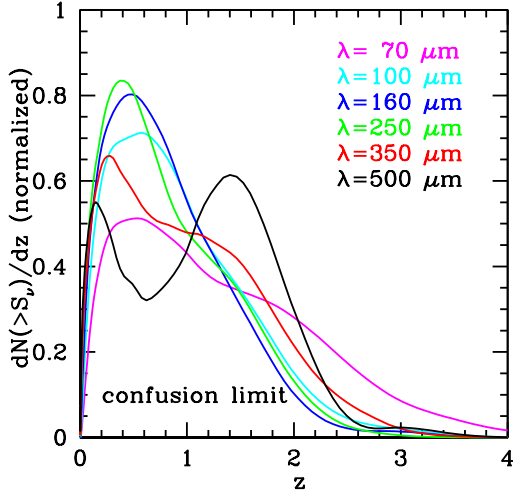


Figure 6. Redshift distributions for galaxies brighter than the predicted confusion limits in each *Herschel* band, as indicated in the key. The redshift distributions are all normalized to unit area under the curve.

redshifting of the SED combined with the negative slope of the dust SED longwards of the peak counteracts the dimming due to the increasing luminosity distance, and makes higher redshift galaxies more easily visible than lower redshift galaxies. This effect is already well known from longer-wavelength sub-mm observations at $850\mu\text{m}$ (e.g. Hughes et al. 1998).

The next figure, Fig. 7, shows the predicted redshift distributions at different wavelengths for all of the deep survey tiers listed in Table 2. In this figure, the redshift distributions are normalized to the expected number of galaxies in the survey area, to allow an easier estimate of the number of galaxies predicted in different redshift ranges for each of the surveys. Fig. 8 examines the redshift distributions for these deep surveys in more detail, showing the separate contributions of quiescent and bursting galaxies to the total redshift distributions for selected survey tiers at particular wavelengths. We show two survey tiers (GOODS-Herschel and HERMES-L1) and three wavelengths (100, 250 and $500\mu\text{m}$) to illustrate the general behaviour. In all cases, we see that the quiescent galaxies dominate the distribution at low redshifts and the bursts at high redshifts, reflecting the higher luminosities of the bursts. We also see that the bursts become more dominant overall at longer wavelengths in the deep surveys, due to the effects of the negative k-correction.

Finally, in Fig. 9, we show the predicted redshift distributions for the shallower but wider-area ATLAS survey. Out of the 5 wavelengths in this survey, the largest number of galaxies should be seen at $250\mu\text{m}$. The median redshift for galaxies brighter than the flux limit is also largest at this wavelength ($z_{50} \approx 0.4$), with 20,000 galaxies at $z > 1.3$ and ~ 1000 galaxies at $z > 2$. The redshift distribution is broader at the longer wavelengths (250- $500\mu\text{m}$) compared to the shorter wavelengths (100 and $160\mu\text{m}$), again as a result of the negative k-correction at longer wavelengths.

5 PHYSICAL PROPERTIES OF *Herschel* GALAXIES

Having presented predictions for directly observable quantities (fluxes and redshifts) in the previous section, we now move on to the predicted physical properties of the galaxies detected in *Her-*

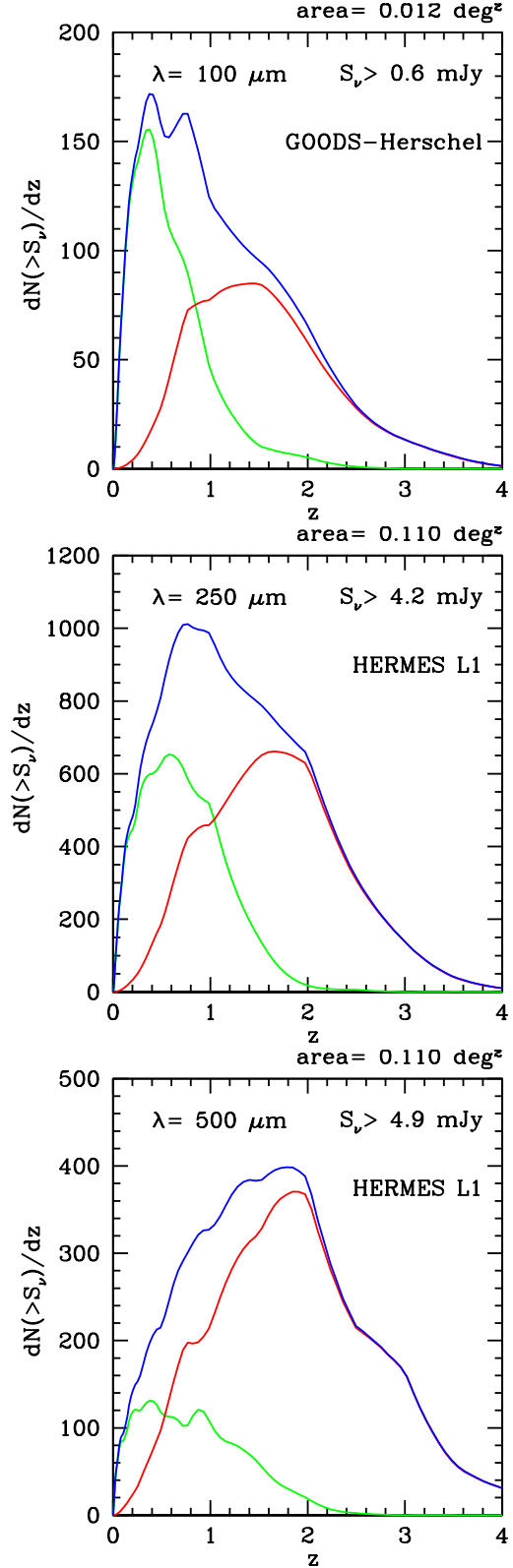


Figure 8. Redshift distributions for galaxies brighter than the flux limits of the deepest planned blank-field surveys, showing the total (blue), together with the contributions of burst (red) and quiescent (green) galaxies. (a) GOODS-Herschel at $100\mu\text{m}$. (b) HERMES-L1 at $250\mu\text{m}$. (c) HERMES-L1 at $500\mu\text{m}$.

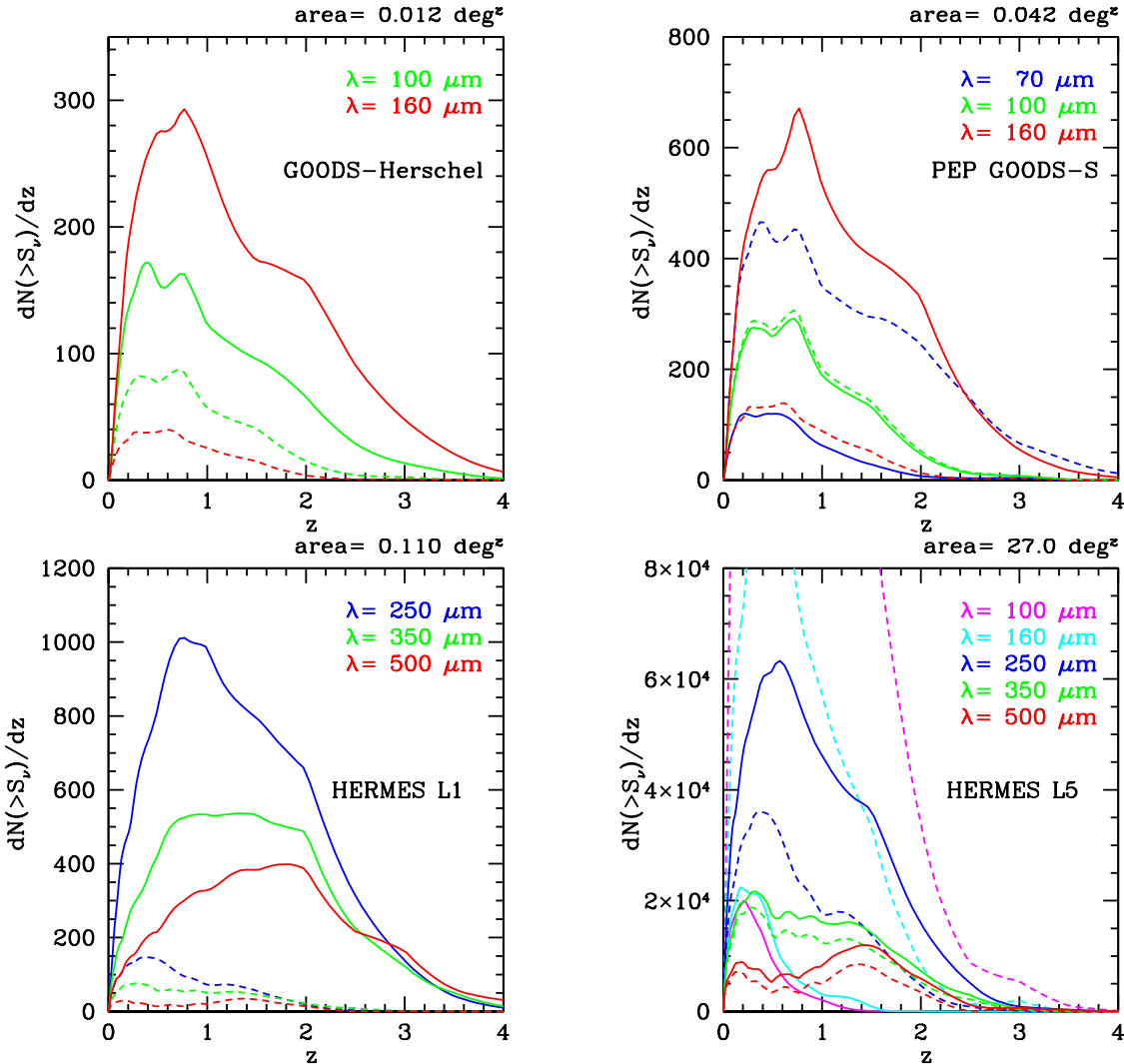


Figure 7. Redshift distributions in planned deep blank-field surveys. (a) GOODS-Herschel. (b) PEP GOODS-S. (c) HERMES L1 (CDFs). (d) HERMES L5. In each panel, redshift distributions for the different wavelengths are shown in different colours, as indicated in the key. The solid lines show the redshift distribution for galaxies brighter than the nominal flux limit of the survey, while the dashed lines show the redshift distribution for galaxies brighter than the predicted confusion limit. In all panels, the redshift distributions are normalized so that the area the curve is equal to the predicted number of galaxies in the survey area.

schel surveys as a function of flux and redshift. We focus here on four properties of central physical importance: the total IR luminosity, L_{IR} , the star formation rate, SFR, the stellar mass, M_{star} , and the host dark halo mass, M_{halo} .

In Fig. 10, we plot the median total IR luminosity L_{IR} (integrated over the wavelength range 8–1000 μm) against flux, for three different *Herschel* bands (one in each panel), for galaxies at one of six different redshifts ($z = 0.25, 0.5, 1, 2, 3, 4$, as indicated by the different colours shown in the key). We have chosen wavelengths of 100, 250 and 500 μm to be representative of the six imaging bands. The “error bars” on each line show the 10-90% range of the distribution at each flux and redshift. We have also plotted vertical lines showing the nominal flux limits of the different Key Project surveys discussed in the previous section, as well as the predicted confusion limit at each wavelength. As mentioned previously, L_{IR} essentially measures the total luminosity of dust emission from a galaxy. For galaxies with significant recent star formation, L_{IR} is powered mostly by far-UV radiation from massive young stars, and

it thus provides a tracer of the dust-obscured star formation rate for high mass ($m \gtrsim 5M_{\odot}$) stars. The actual conversion factor between L_{IR} and the total SFR (integrated over all stellar masses) depends both on the fraction of the far-UV light from young stars which is absorbed by dust (which is typically high) and on the IMF. We see from Fig. 10 that at each *Herschel* wavelength and each redshift, there is an approximately linear relationship between L_{IR} and the flux in that band with only modest scatter ($\sim 0.2\text{dex}$). This simply reflects the fact that the *Herschel* bands directly probe the rest-frame far-IR wavelengths which dominate L_{IR} , and that the shape of the far-IR SED shows only modest galaxy-to-galaxy variation at a given redshift, with only a weak dependence on L_{IR} . The zero-point of this relation between L_{IR} and flux obviously depends on the SED shape and on the effects of the luminosity distance and the k-correction; the zero-point changes with redshift less at longer wavelengths (over the range $z = 0.5 - 4$, it increases by ~ 2.5 dex at 100 μm and by ~ 1.5 dex at 500 μm), reflecting the effect of the negative k-correction at the longer wavelengths.

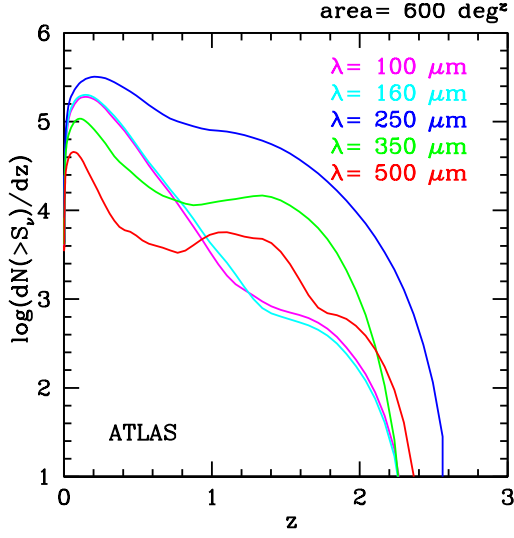


Figure 9. Redshift distributions at 100, 160, 250, 350 and 500 μm at the flux limits of the ATLAS survey. Different wavelengths are shown by different colours, as indicated in the key. The distributions are all normalized so that the integral over the distribution is equal to the expected number of galaxies in the survey area. Note that in this case the log of the redshift distribution is plotted.

One of the main goals of *Herschel* will be to measure the evolution of the cosmic density of dust-obscured star formation, and for this purpose it is interesting to know which *Herschel* wavelength will probe to the faintest L_{IR} at each redshift, since the latter will determine what fraction of the total IR luminosity density is actually resolved into identified objects at that redshift. We see from Fig. 10 that if source confusion sets a hard limit to identifying individual sources, then surveys at 100 μm will probe to the faintest L_{IR} , ranging from $\sim 10^{10.1} h^{-2} L_{\odot}$ at $z = 0.5$ to $\sim 10^{12.4} h^{-2} L_{\odot}$ at $z = 4$. On the other hand, if all of the planned Key Project surveys manage to resolve objects down to their nominal flux limits (even where these are below confusion), then the GOODS-Herschel survey at 160 μm will probe faintest (down to $L_{\text{IR}} \sim 10^{9.5} h^{-2} L_{\odot}$ at $z = 0.5$ and $\sim 10^{11.9} h^{-2} L_{\odot}$ at $z = 4$). Of the surveys in the SPIRE bands at 250-500 μm , those at 250 μm will probe down to the lowest L_{IR} whether confusion can be circumvented or not, except at the highest redshifts, $z \gtrsim 2 - 3$, for which the 500 μm band becomes more sensitive due to the negative k-correction effect.

Fig. 11 is similar to Fig. 10, except that the SFR rather than L_{IR} is plotted against flux. As already described, the relation between L_{IR} and SFR depends on the fraction of UV light from young stars absorbed by dust and on the IMF. In particular, in our model, L_{IR}/SFR is about 4 times larger for star formation in bursts with the top-heavy ($x = 0$) IMF compared to the stars forming quiescently in disks with the Kennicutt (1983) IMF. The proportion of star formation associated with the burst mode on average increases with increasing L_{IR} , and for this reason the relation between SFR and flux is shallower than a linear proportionality. The scatter is also somewhat larger than for the L_{IR} -flux relation. We see from the figure that, at the confusion limit, *Herschel* surveys should probe down to SFRs $\sim 1 h^{-1} M_{\odot} \text{yr}^{-1}$ at $z = 0.5$ and $\sim 10^2 h^{-1} M_{\odot} \text{yr}^{-1}$ at $z = 4$, the lowest limits being achieved at 100 μm . The planned Key Project surveys may improve on this by factors ~ 2 if they can get below the confusion limit.

Fig. 12 is analogous to the previous two figures, but now with

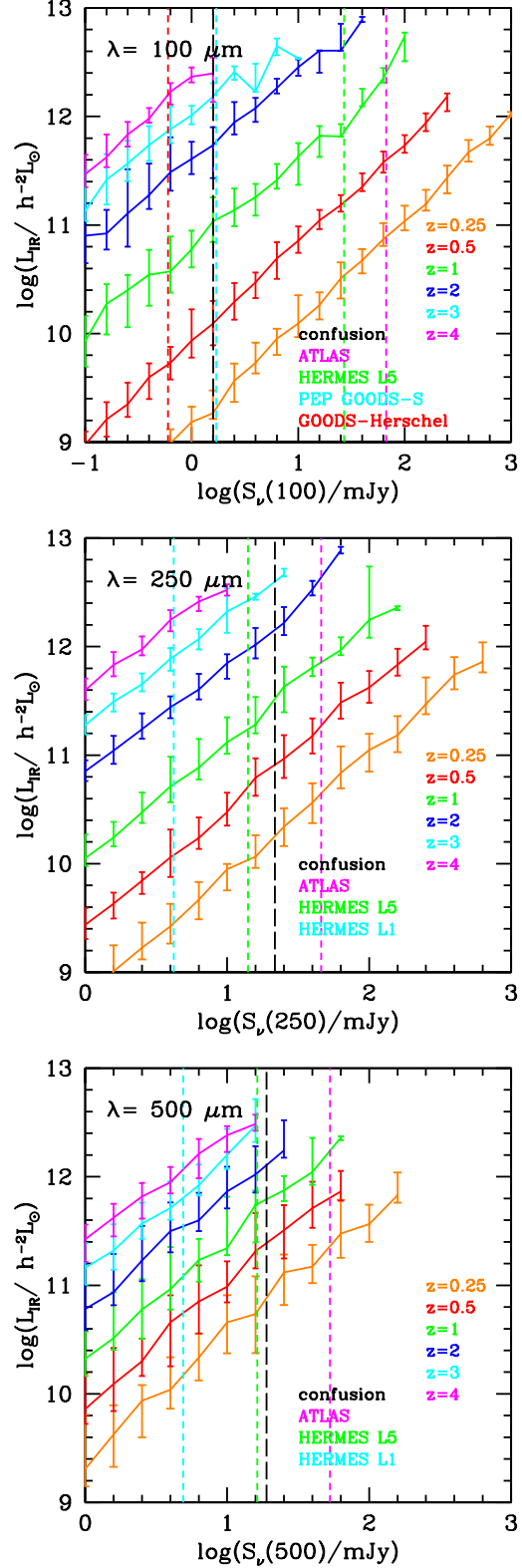


Figure 10. Median total IR (8-1000 μm) luminosity, L_{IR} , vs flux at 100, 250 and 500 μm for galaxies selected at different redshifts, shown by different colours as indicated in the key. The “error bars” on the lines show the 10-90% range. The vertical dashed black line shows the predicted confusion limit at each wavelength, while the vertical dashed coloured lines show the nominal flux limits for different planned surveys, as indicated in the key.

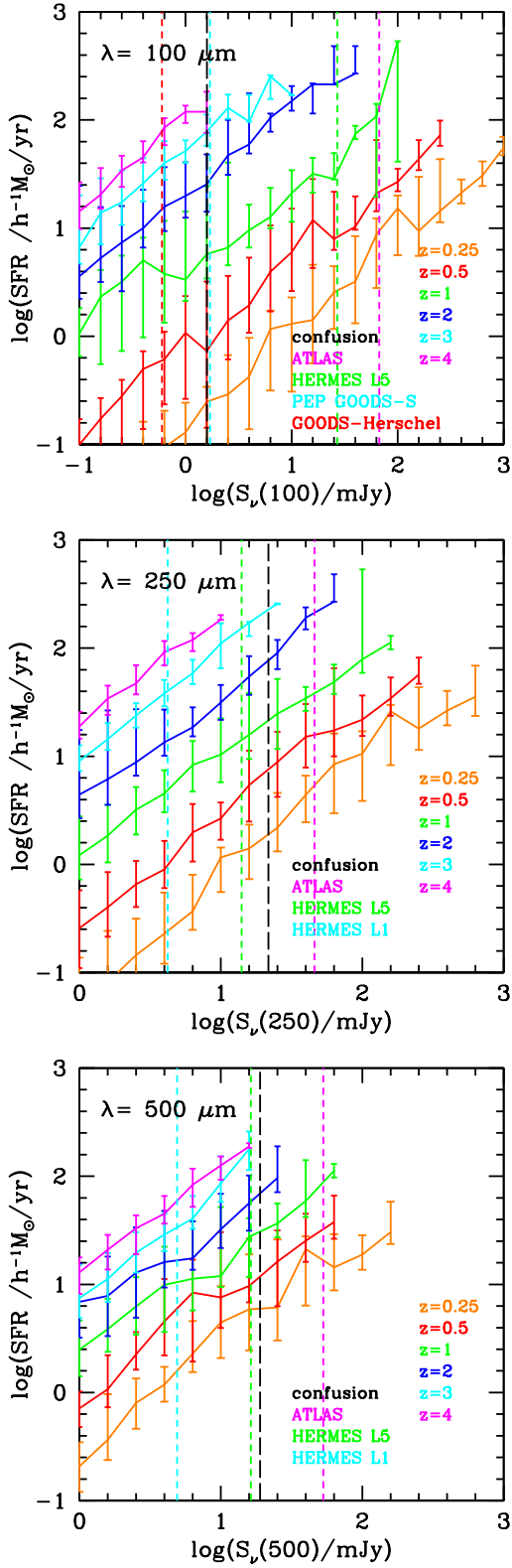


Figure 11. Median total SFR vs flux at 100, 250 and 500 μm for galaxies selected at different redshifts. The different lines are as described for Fig.10.

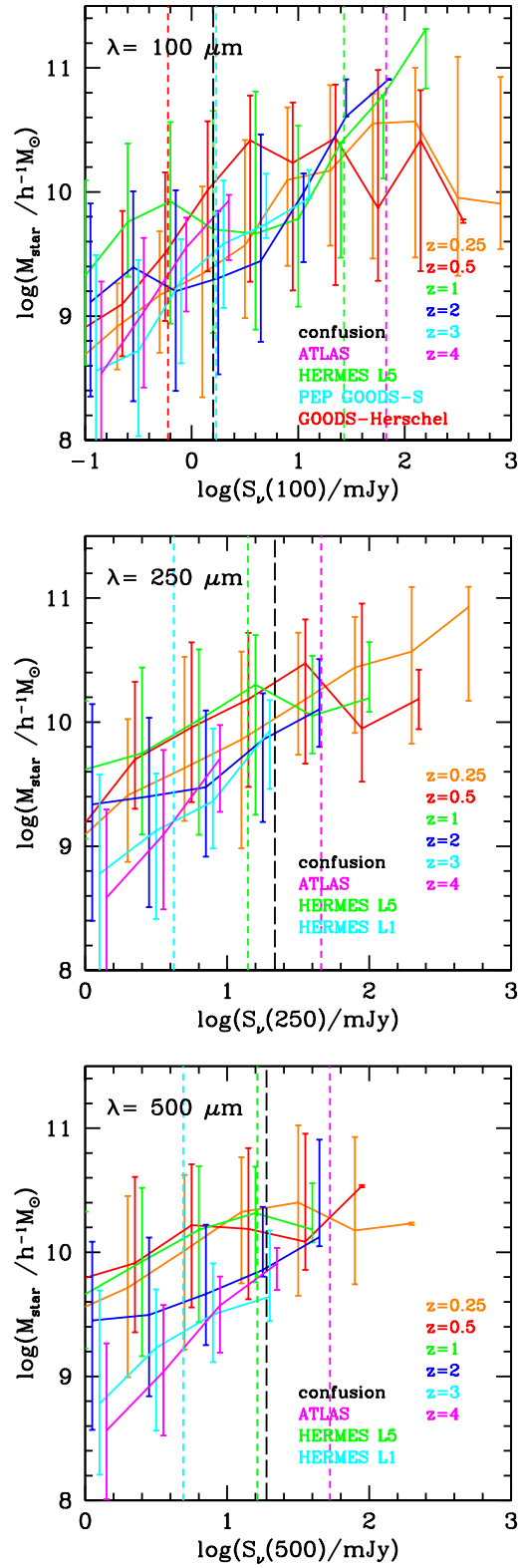


Figure 12. Median stellar mass vs flux at 100, 250 and 500 μm for galaxies selected at different redshifts. For clarity, we have introduced small horizontal offsets between the lines plotted for different redshifts.

the stellar mass M_{star} plotted against flux. In this case, the relation is far from linear, and has much larger scatter than for L_{IR} or SFR. This is not surprising, since the *Herschel* flux is proportional to the emission from dust heated mostly by massive young stars, while the stellar mass includes stars of all ages and masses. Since the galaxies in our model have complex star formation histories, there is no simple relation between the current star formation rate and the total mass of stars formed over the history of the galaxy. The galaxies found in *Herschel* surveys should have stellar masses over the range $M_{star} \sim 10^9 - 10^{11} h^{-1} M_{\odot}$, with a weaker dependence on redshift at a given flux than is typically seen for the SFR.

Finally, in Fig. 13, we show the relation between the host dark halo mass M_{halo} and flux in the *Herschel* bands. Here we see that the median halo mass depends much more weakly on flux or redshift (and with a larger scatter) than either M_{star} or SFR, especially at the longer wavelengths. This reflects the fact that in our model the relation between far-IR luminosity and halo mass is even more indirect than for the stellar mass, especially due to the dominance of transient bursts at the higher luminosities. This produces the relatively flat trend of median halo mass with *Herschel* flux. The weak dependence on redshift is because halos of a given mass on average host higher SFRs at higher z , which compensates for the larger luminosity distance. We see from Fig. 13 that the galaxies found in the Key Project cosmological surveys should typically have halo masses $M_{halo} \sim 10^{12} h^{-1} M_{\odot}$. This will have important implications when we consider the clustering of *Herschel* galaxies in §8.

We have also investigated the dependence of the stellar bulge-to-total mass ratio B/T and the cold gas mass M_{gas} on flux in the *Herschel* bands. For brevity, we only show results for the $250\mu\text{m}$ band in Fig. 14. We find that the 10-90% range for B/T covers nearly the whole possible range $0 \leq B/T \leq 1$ at most fluxes and redshifts of interest in the planned *Herschel* cosmological surveys, i.e. there is no strong preference for one morphological type over another. The exception to this is at low fluxes and low redshifts, where most sources have $B/T \lesssim 0.5$. This reflects the fact that the galaxies found in these surveys should be a mixture of quiescently star-forming disk galaxies and starbursts triggered by galaxy mergers, and even though the most luminous galaxies in the far-IR are predicted to be bursts, these can be triggered by either major or minor mergers, producing a bursting galaxy which can be either bulge or disk dominated. There is a trend for the median B/T to increase with flux at a given redshift, presumably reflecting an increase in the fraction of bursts triggered by major mergers. We illustrate these trends in the top panel of Fig. 14. For the cold gas mass M_{gas} , shown in the lower panel of Fig. 14, we find a correlation with flux which is weaker than linear, and also fairly weakly dependent on redshift. We predict that the galaxies found in the *Herschel* cosmological surveys should typically have gas masses $\sim 10^{10} h^{-1} M_{\odot}$, which implies that many of them should have CO emission from their molecular gas which is detectable by current telescopes (e.g. Solomon & Vanden Bout 2005).

6 MULTI-WAVELENGTH PREDICTIONS

Obtaining multi-wavelength data complementary to that from *Herschel* itself will be crucial for achieving the science goals of the cosmological surveys. Such data will be essential for obtaining identifications and accurate positions of the sources, for obtaining accurate redshifts, and for learning more about the physical nature of these galaxies. It is therefore of interest to see what the model predicts for the observability of *Herschel* sources at other wavelengths.

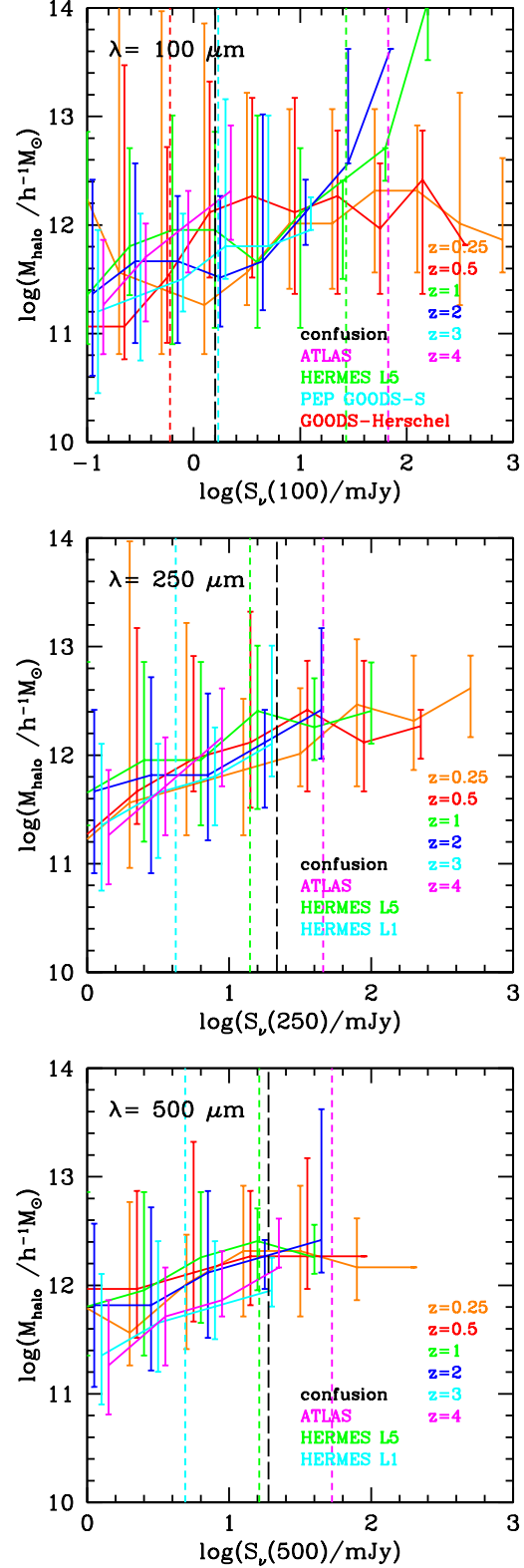


Figure 13. Median halo mass vs flux at 100, 250 and $500\mu\text{m}$ for galaxies selected at different redshifts. The different lines are as described for Fig.10. For clarity, we have introduced small horizontal offsets between the lines plotted for different redshifts.

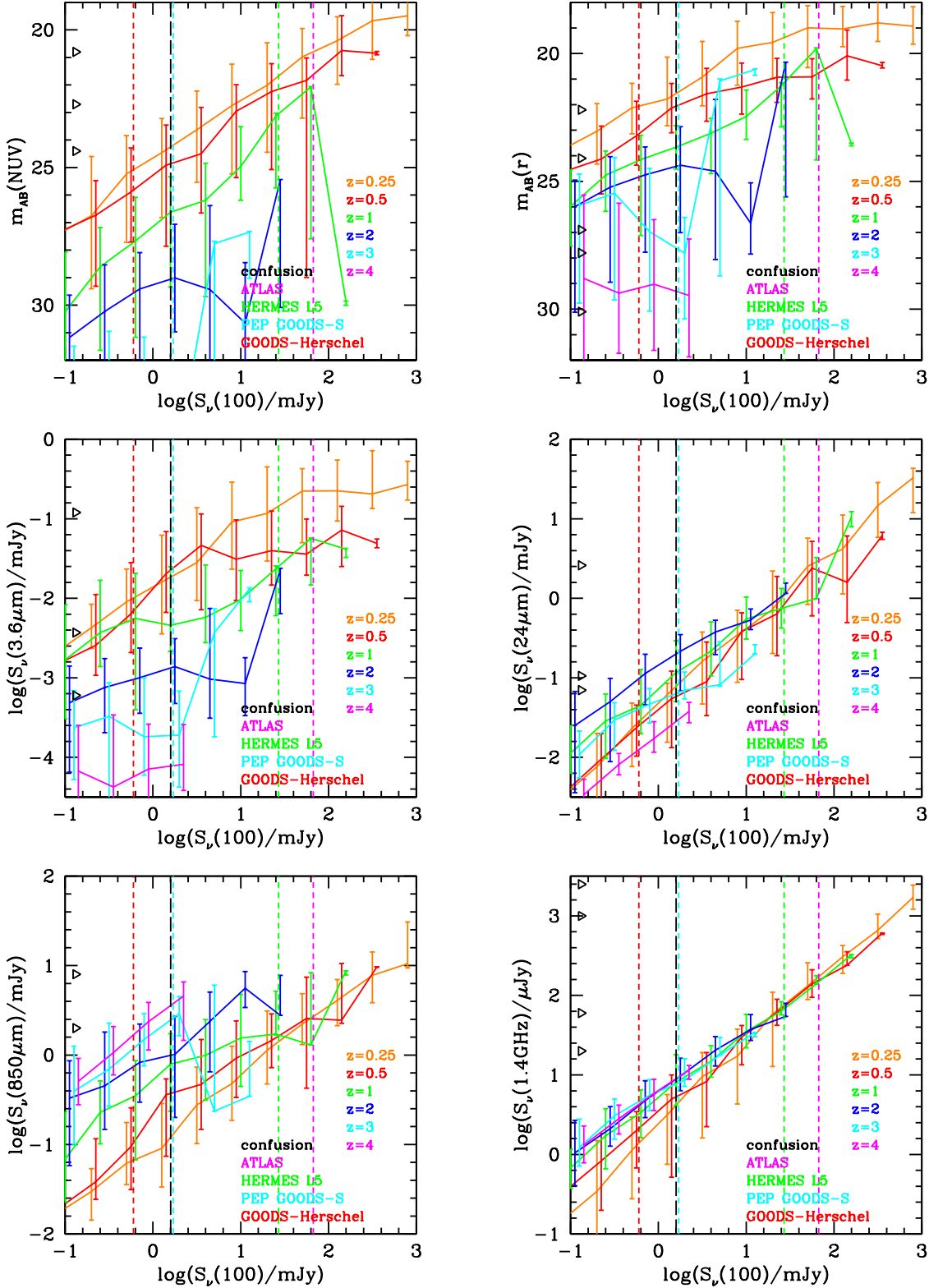


Figure 15. Median fluxes or magnitudes at other wavelengths for galaxies selected at $100\mu\text{m}$. (a) GALEX NUV. (b) r-band. (c) IRAC $3.6\mu\text{m}$. (d) MIPS $24\mu\text{m}$. (e) SCUBA $850\mu\text{m}$. (f) 1.4GHz. The triangles next to the the y-axes in these panels indicate the magnitude or flux limits for the different surveys which are discussed in the text. For clarity, we have introduced small horizontal offsets between the lines plotted for different redshifts.

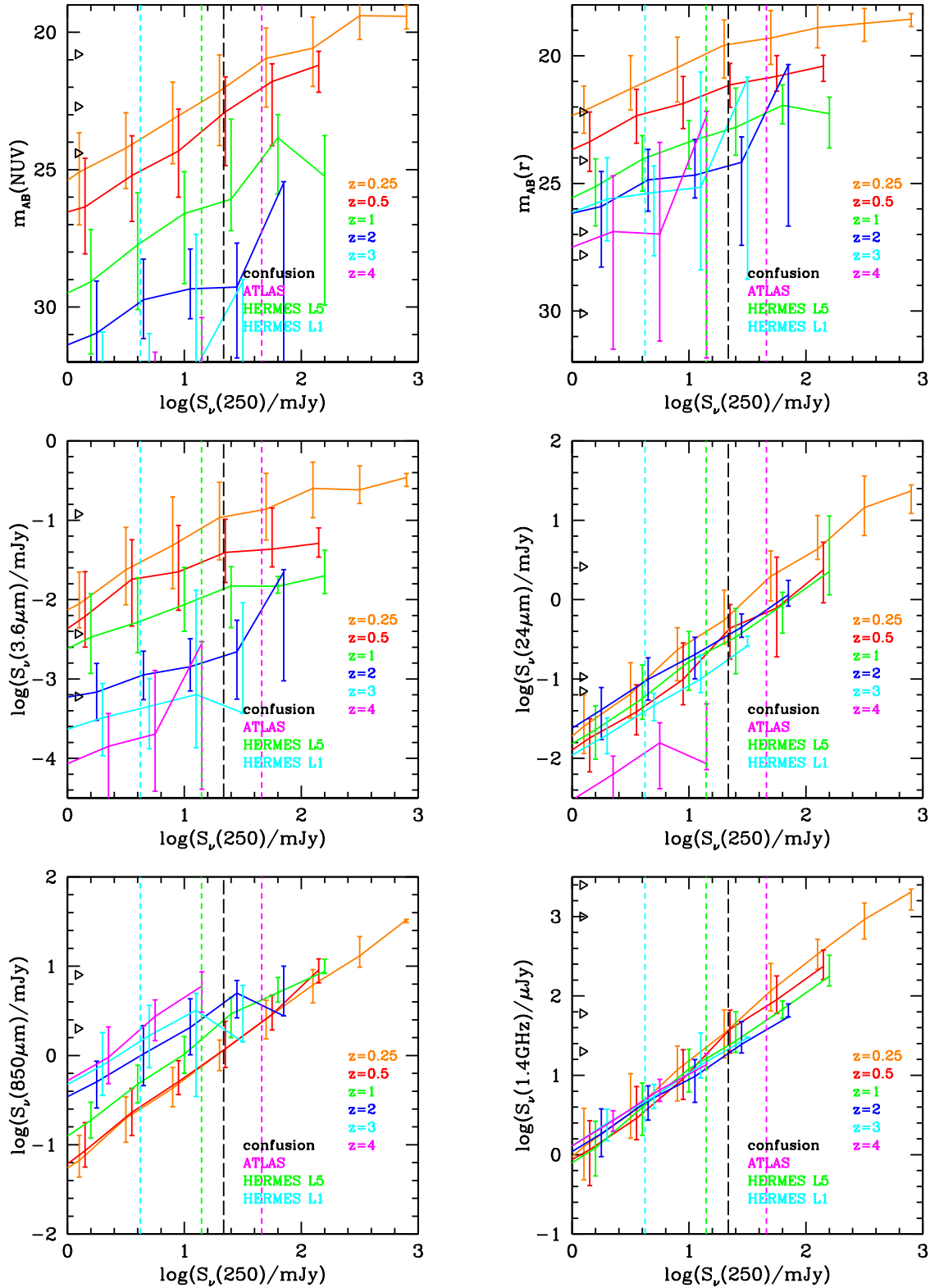


Figure 16. Median fluxes or magnitudes at other wavelengths for galaxies selected at $250\mu\text{m}$. (a) GALEX NUV. (b) r-band. (c) IRAC $3.6\mu\text{m}$. (d) MIPS $24\mu\text{m}$. (e) SCUBA $850\mu\text{m}$. (f) 1.4GHz . The triangles indicate the flux limits for different surveys, as in Fig. 15. For clarity, we have introduced small horizontal offsets between the lines plotted for different redshifts.

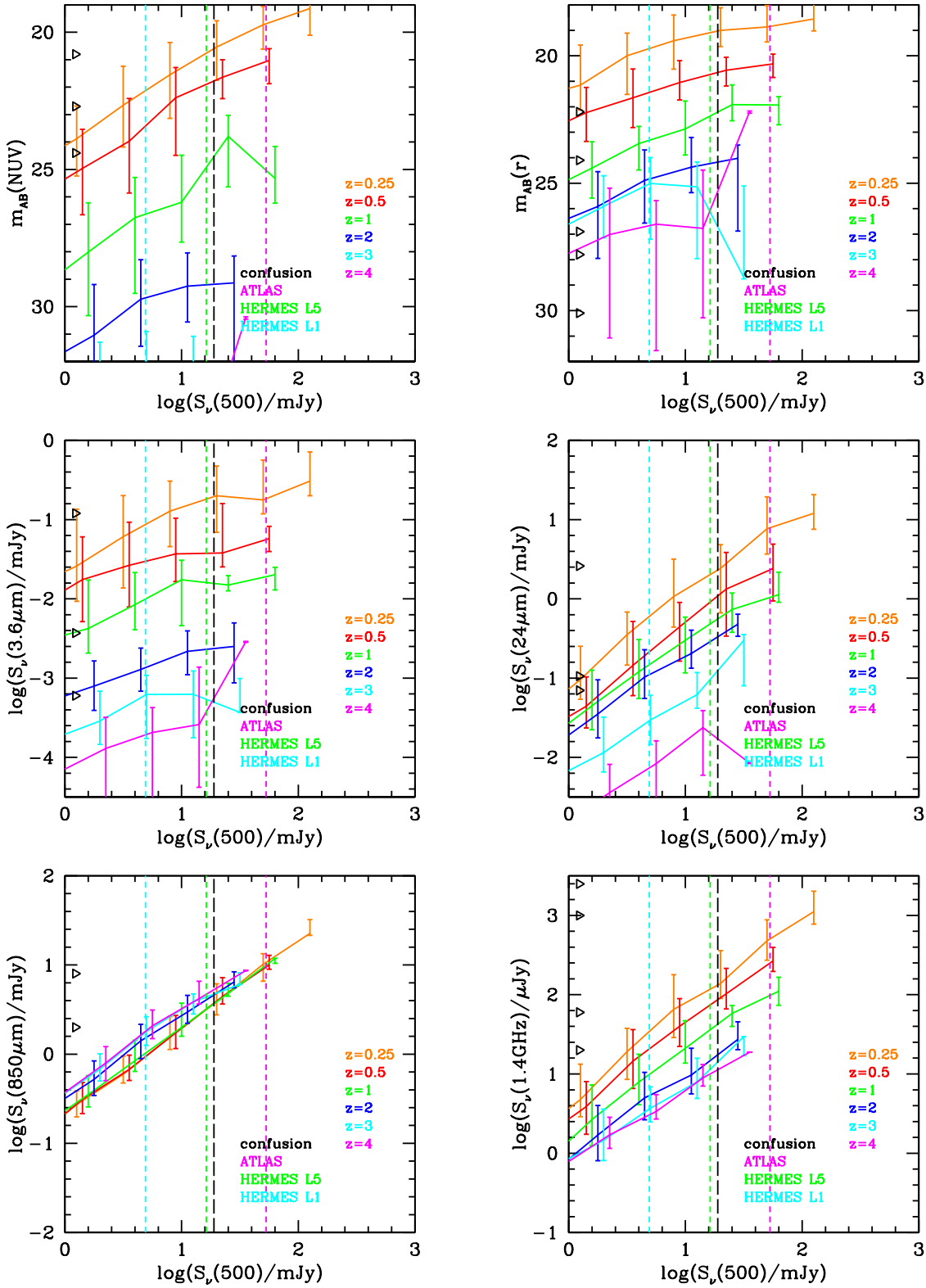


Figure 17. Median fluxes or magnitudes at other wavelengths for galaxies selected at $500\mu\text{m}$. (a) GALEX NUV. (b) r-band. (c) IRAC $3.6\mu\text{m}$. (d) MIPS $24\mu\text{m}$. (e) SCUBA $850\mu\text{m}$. (f) 1.4GHz. The triangles indicate the flux limits for different surveys, as in Fig. 15. For clarity, we have introduced small horizontal offsets between the lines plotted for different redshifts.

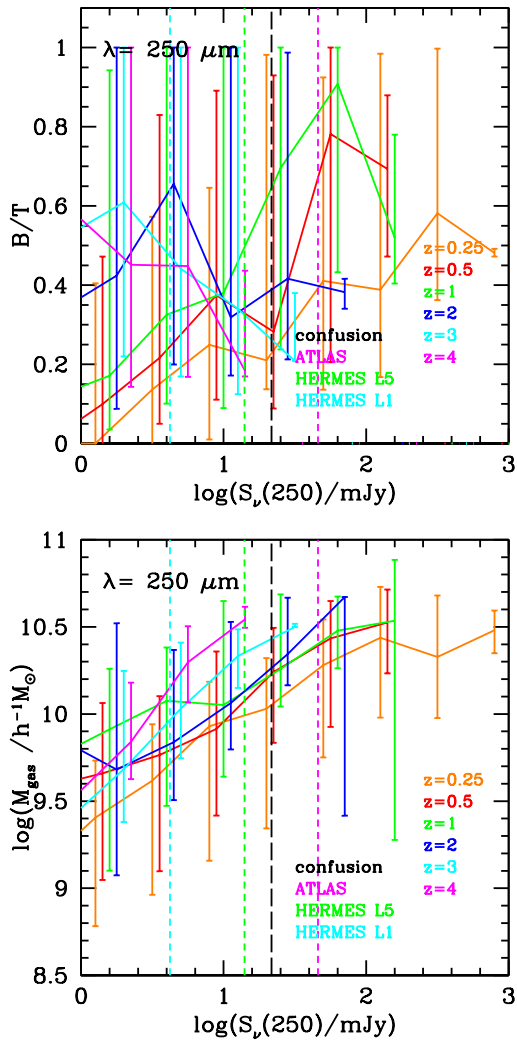


Figure 14. Median bulge-to-total stellar mass ratio B/T and cold gas mass vs flux at $250 \mu\text{m}$ for galaxies selected at different redshifts. The different lines are as described for Fig.10. For clarity, we have introduced small horizontal offsets between the lines plotted for different redshifts.

In Figs. 15, 16 and 17, we show predicted fluxes or AB magnitudes at wavelengths from the UV to the radio, plotted against the *Herschel* flux at either 100 or 250 or $500 \mu\text{m}$. Specifically, we consider the GALEX *NUV* filter (centred at $\lambda = 0.23 \mu\text{m}$), the SDSS *r*-band (centred at $\lambda = 0.62 \mu\text{m}$), the *Spitzer* 3.6 and $24 \mu\text{m}$ bands, the SCUBA $850 \mu\text{m}$ band, and the VLA 1.4GHz band. The observer-frame *NUV*, $24 \mu\text{m}$, $850 \mu\text{m}$ and 1.4GHz bands in the main trace recent star formation, while the observer-frame $3.6 \mu\text{m}$ band traces older stars, and the observer-frame *r*-band traces older stars at low redshift but younger stars at high redshift (when it corresponds to the rest-frame UV). The predicted median fluxes at 0.23, 24 and $850 \mu\text{m}$ and at 1.4 GHz generally track the fluxes in the *Herschel* bands fairly well, but with zero-points which can depend strongly on redshift, depending on the wavelength. This is particularly the case for the GALEX *NUV* band, for which the flux drops rapidly with redshift at $z \gtrsim 1.5$ when the band falls shortward of the Lyman break in the rest frame. (Note that we include the effects of absorption by the intervening IGM when we calculate the UV and optical magnitudes.) The redshift dependence of the ze-

ropoints is generally least at 1.4 GHz and $24 \mu\text{m}$. As expected, the correlation with the *Herschel* flux is much weaker for the *r* and $3.6 \mu\text{m}$ bands, which are more sensitive to stellar mass than to the SFR.

For comparison, we note the approximate flux or magnitude limits for some of the main surveys at these wavelengths (the flux limits for these surveys are also indicated by triangles along the y-axis in Figs. 15-17):

GALEX NUV: All-sky Imaging Survey (AIS) $m_{AB} = 20.8$; Medium Imaging Survey (MIS) $m_{AB} = 22.7$; Deep Imaging Survey (DIS) $m_{AB} = 24.4$ (Morrissey et al. 2007).

SDSS r: SDSS Legacy Survey $m_{AB} = 22.2$ (Abazajian et al. 2009); Subaru Deep Field $m_{AB} = 27.8$ (R_C) (Kashikawa et al. 2004); Hubble Ultra-Deep Field $m_{AB} = 30.1$ (*V* or *i*) (Beckwith et al. 2006); Pan-STARRS PS1 $m_{AB} = 24.1$ in the 3π survey and $m_{AB} = 26.9$ in the Medium Deep Survey (MDS) (Chambers 2006).

Spitzer 3.6 μm: SWIRE $S_\nu = 3.7 \mu\text{Jy}$ (Lonsdale et al. 2004); GOODS $S_\nu = 0.6 \mu\text{Jy}$ (Dickinson et al. 2003). Also the WISE satellite will survey the whole sky to $S_\nu = 120 \mu\text{Jy}$ at a wavelength of $3.3 \mu\text{m}$ (Wright et al. 2007).

Spitzer 24 μm: SWIRE $S_\nu = 106 \mu\text{Jy}$ (Lonsdale et al. 2004); GOODS $S_\nu = 70 \mu\text{Jy}$ (Chary et al. 2004). Also WISE will survey the whole sky to $S_\nu = 2600 \mu\text{Jy}$ at a wavelength of $23 \mu\text{m}$ (Wright et al. 2007).

SCUBA 850 μm: HDF $S_\nu = 2 \text{mJy}$ (Hughes et al. 1998); SHADES $S_\nu = 8 \text{mJy}$ (Mortier et al. 2005) SASSy⁸ $S_\nu = 150 \text{mJy}$.

1.4 GHz: NVSS $S_\nu = 2.5 \text{mJy}$ (Condon et al. 1998); FIRST $S_\nu = 1 \text{mJy}$ (Becker et al. 1995); Phoenix $S_\nu = 60 \mu\text{Jy}$ (Hopkins et al. 2003); SSA 13 $S_\nu = 20 \mu\text{Jy}$ (Fomalont et al. 2006).

7 UNVEILING THE COSMIC STAR FORMATION HISTORY

Since the discovery of the far-IR background by COBE, it has been known that the bulk of star formation over the history of the Universe has been obscured by dust. One of the primary goals of *Herschel* is to resolve the far-IR background into individual sources and hence determine the amount of dust-obscured star formation at different cosmic epochs. How well *Herschel* will be able to do this depends on the distribution of the total IR emissivity, ϵ_{IR} , (i.e. the mean luminosity density per comoving volume) over sources of different luminosities and over redshift, and how far down in total IR luminosity, L_{IR} , *Herschel* surveys are able to probe at different redshifts. This section is devoted to investigating the implications of our models for this key issue.

We start by showing in the top left panel of Fig. 18 the cosmic star formation history predicted by our model, both the total star formation density and the separate contributions to this from ongoing starbursts and from quiescently star-forming galactic disks (this was earlier shown in Baugh et al. 2005). The total SFR density increases by a factor ≈ 6 from $z = 0$ to $z = 2.5$, and then declines very gradually to higher z . We see that the quiescent mode of star formation dominates the SFR density at redshifts $z \lesssim 3$ probed by *Herschel*, while the burst mode dominates at higher redshifts.

⁸ <http://www.jach.hawaii.edu/JCMT/surveys/sassy/>

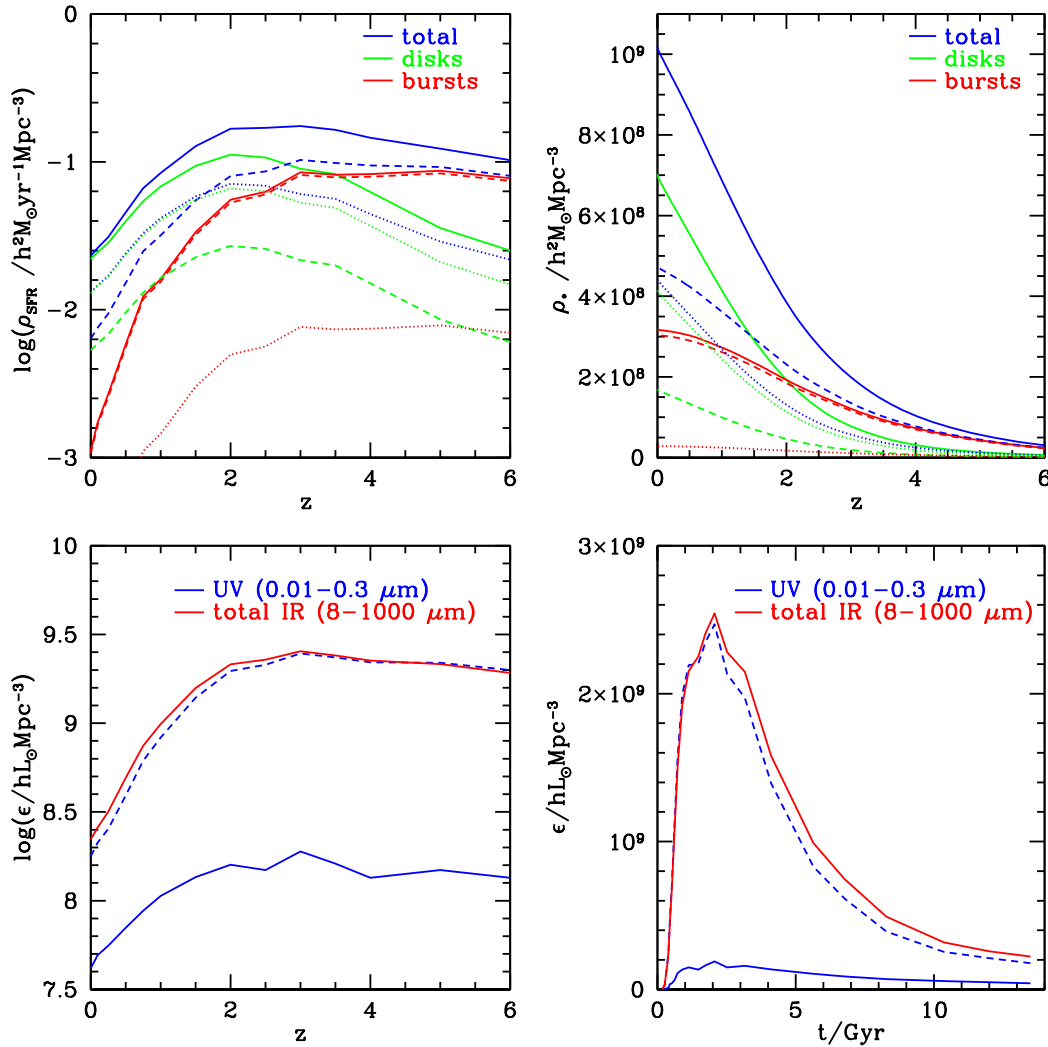


Figure 18. (a) Cosmic SFR history, showing the total SFR density (blue) and the separate contributions from bursts (red) and quiescent disks (green). The solid lines show the total SFR density integrated over all stellar masses, while the dashed lines show the SFR density in massive stars ($m > 5M_{\odot}$). The dotted lines show the rate of build-up of stellar mass in long-lived stars and remnants, after allowing for recycling of gas to the ISM. (b) The time integral of SFR density from $t = 0$ up to $t(z)$. The line colours and styles are identical to (a). (c) Evolution of luminosity density in rest-frame UV (with and without dust, shown by the solid and dashed lines) and in the mid/far-IR. (d) The same as in (c), except plotted on a linear scale against cosmic time.

We also show by dashed lines in the same panel the star formation density in massive stars only, which we define as stars with masses $m > 5M_{\odot}$, which have lifetimes $< 1 \times 10^8 \text{yr}$. We choose this mass range because, when integrated over the whole galaxy population, such stars dominate the UV emissivity from galaxies, and also dominate the heating of the dust which powers most of the mid- and far-IR emission from galaxies. The two IMFs in our model (assumed to cover the stellar mass range $0.15 < m < 120M_{\odot}$) have very different fractions of their initial stellar mass in high mass stars: we find $f(m > 5M_{\odot}) = 0.24$ for the Kennicutt IMF assumed for quiescent star formation, and $f(m > 5M_{\odot}) = 0.96$ for the top-heavy $x = 0$ IMF assumed for bursts. (For comparison, $f(m > 5M_{\odot}) = 0.22$ for a Salpeter IMF covering the same mass range.) The SFR density for massive stars therefore evolves more strongly than that for all stars, increasing by a factor ≈ 15 from $z = 0$ to a peak at $z \approx 3$. For massive star formation, the burst mode already dominates the quiescent mode at $z \gtrsim 1$. Finally, the dotted lines in the top panel show the rate of

build-up of stellar mass in long-lived stars and stellar remnants, after accounting for the mass returned to the ISM by dying stars. The fraction of the initial stellar mass returned in this way is called the recycled fraction, and depends on the IMF, having values of 0.41 for the Kennicutt IMF and 0.91 for the $x = 0$ IMF. We see that, after allowing for recycling, the quiescent mode of star formation dominates the build-up of stellar mass even at the highest redshifts plotted.

We show in the top right panel of Fig. 18 the time integral of the SFR density from $t = 0$ up to redshift z for the different components. Focussing on the integral up to $z = 0$, we see that, integrated over the history of the Universe, 31% of all star formation is predicted to occur in the burst mode, but at the present day this fraction is only 4.8%. For high mass ($m > 5M_{\odot}$) stars, 64% of star formation happened in the burst mode over the history of the universe, while the present-day fraction is 17%. The burst mode is thus more important for high mass star formation. However, after accounting for recycling of mass from dying stars, we find that the

fraction of the present-day stellar mass produced by the burst mode is only 6.4%.

In the lower panels of Fig. 18 we show how the model SFR density evolution translates into the evolution of the cosmic emissivity from galaxies in the UV (defined here as the integral over the wavelength range $0.01 - 0.3\mu\text{m}$) and the total mid/far-IR (integrated over the range $8 - 1000\mu\text{m}$, as previously). The UV emissivity is plotted both with and without dust extinction. The unextincted UV and total IR emissivities both increase by factors ~ 10 from $z = 0$ to $z = 3$, and then remain approximately constant up to $z = 6$. This difference in redshift dependence compared to that for the total SFR density is because both the UV and total IR emissivities are powered mostly by massive stars ($m \gtrsim 5M_\odot$), and the burst mode of star formation produces a larger fraction of such stars than the quiescent mode. We see that the effect of dust extinction on the UV emissivity is predicted to be very large - integrated over the history of the Universe, 90% of the UV energy is predicted to be absorbed by dust. This fraction increases from 77% at $z = 0$ to 87% at $z = 1$ and 92% at $z = 6$. This emphasizes how essential it is to measure the cosmic evolution of the total IR emissivity in order to measure directly the cosmic SFR history, free of uncertain observational estimates of UV dust extinction. The total IR emissivity is seen to be very similar to the unextincted far-UV emissivity at all redshifts, which just reflects the fact that most of the far-UV radiation is absorbed by dust, and that heating of the dust by longer wavelength (optical and near-IR) radiation from stars is a minor contribution to the total when integrated over the whole galaxy population. (The fraction of the IR emissivity due to heating by longer wavelength radiation is predicted to be around 20% integrated over the history of the Universe, dropping from 40% at $z = 0$ to only 20% at $z = 1.5$ and 10% at $z = 3$.)

We next consider the fraction of the total IR emissivity, ϵ_{IR} , which is produced by galaxies brighter than total luminosity L_{IR} for different redshifts. This is obtained by integrating over the total IR luminosity function, which was shown in Fig. 2. The results are shown in the top and bottom panels of Fig. 19. The top panel shows the fraction of the IR emissivity in galaxies brighter than L_{IR} as a function of L_{IR} for different redshifts, while the bottom panel shows the same fraction as a function of redshift for a number of different minimum luminosities. We see from the top panel that the value of L_{IR} above which 50% of the IR emissivity is contributed increases with increasing z , from $3 \times 10^{10} h^{-2} L_\odot$ at $z = 0$ to $2 \times 10^{11} h^{-2} L_\odot$ at $z = 3$, due to the general brightening in the luminosity function with z discussed in §3. This evolutionary effect partly compensates for the effect of increasing luminosity distance, which generally means that the minimum L_{IR} for which we can detect galaxies in surveys increases with z .

The middle panel in Fig. 19 shows the fraction of star formation occurring in galaxies brighter than L_{IR} , as a function of L_{IR} for different redshifts. We show this both for the total SFR integrated over all stellar masses (solid lines) and for the high-mass ($m > 5M_\odot$) SFR (dashed lines). As a consequence of the bright end of the total IR LF being dominated by bursts with a top-heavy IMF, galaxies brighter than a given L_{IR} account for a larger fraction of the high-mass SFR than of the total SFR. For example, at $z = 3$, galaxies with $L_{IR} > 2 \times 10^{11} h^{-2} L_\odot$ account for 50% of the high-mass SFR but only 36% of the total SFR.

The critical question is: what fraction of the total IR emissivity will different *Herschel* surveys be able to resolve at different redshifts? To answer this, we plot in the top panel of Fig. 20 the fraction of the total IR emissivity ϵ_{IR} produced by galaxies brighter than some flux S_ν as a function of redshift. Each of the six *Herschel*

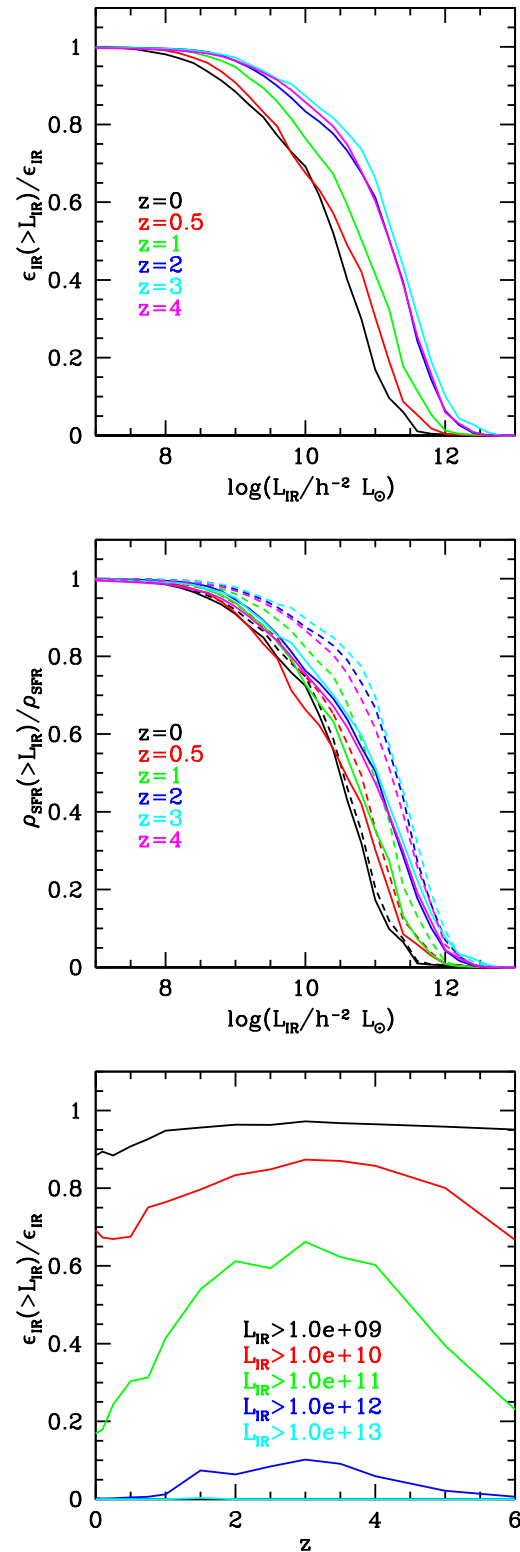


Figure 19. (a) Fraction of total IR luminosity density from galaxies brighter than L_{IR} at different redshifts. (b) Fractions of total SFR (solid lines) and high-mass SFR (dashed lines) from galaxies brighter than L_{IR} at different redshifts. (c) Fraction of total IR luminosity density from galaxies brighter than L_{IR} as function of redshift.

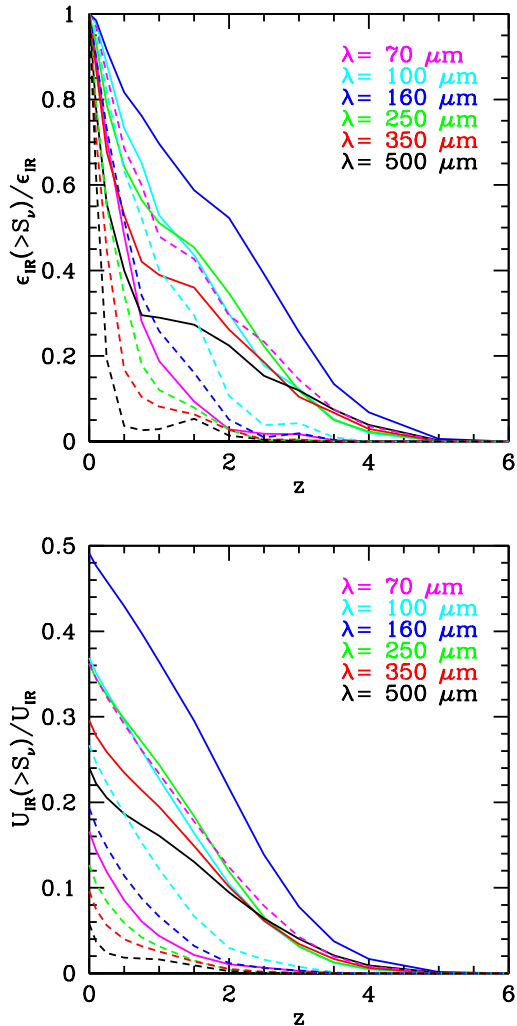


Figure 20. (a) Fraction of IR luminosity density from galaxies brighter than expected *Herschel* survey flux limits at different wavelengths. The solid lines correspond to the faintest nominal flux limit at each wavelength (ignoring confusion) from Table 2, while the dashed lines correspond to the confusion limit at each wavelength from Table 1. (b) Similar to (a), but showing the fraction of the time integral of the IR luminosity density up to redshift z which is in galaxies brighter than flux S_ν in a *Herschel* band.

imaging bands is plotted in a different colour, and for each band we show the result for two different flux limits: the solid line shows the result for the faintest planned flux limit at that wavelength ignoring confusion, taken from the list of surveys in Table 2, while the dashed line shows the result at the estimated confusion limit, taken from Table 1. The lower panel of Fig. 20 instead shows the fraction of the time-integrated emissivity $U_{IR}(z) = \int_0^{t(z)} \epsilon_{IR} dt$ which is resolved at a given flux limit. We see from this figure that if source confusion is ignored (or can be circumvented), then the GOODS-Herschel Ultra-deep survey at $160\mu\text{m}$ (with a planned flux limit of 0.9mJy) should resolve the largest fraction of the total IR emissivity into sources at all redshifts. Integrated over all redshifts, a survey at this flux limit would resolve 49% of all IR emission into sources. On the other hand, if confusion sets a hard limit, then the GOODS-Herschel Ultra-deep survey at $100\mu\text{m}$ (with a confusion limit of 1.6mJy) should instead resolve the largest fraction of the

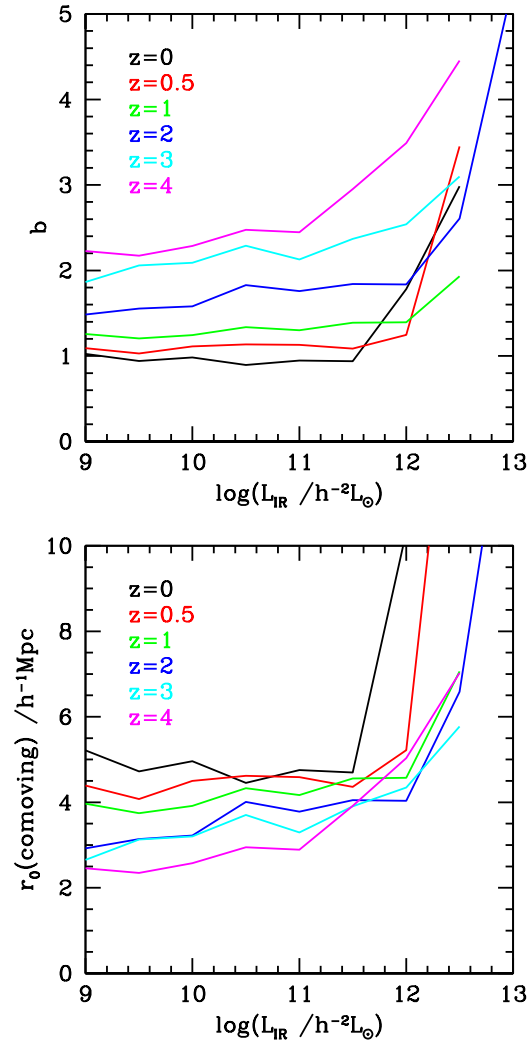


Figure 21. (a) Mean clustering bias b as a function of L_{IR} for galaxies at different redshifts, as indicated in the key. (b) Clustering length r_0 obtained from the bias and power spectrum as function of L_{IR} for different redshifts.

IR emissivity at all redshifts, and a total fraction of 27% when integrated over all redshifts. (In principle, a confusion-limited survey at $70\mu\text{m}$ would resolve a larger fraction, but no such survey is planned). Note that the question we have asked (and answered) here is different from asking what fraction of the present-day cosmic IR background (CIB) is resolved into sources at different fluxes and wavelengths. The energy density in the CIB at $z = 0$ is given by the integral $\int_0^{t_0} \epsilon_{IR}/(1+z) dt$, which differs from the time-integrated emissivity $U_{IR}(z = 0)$ by a factor $1/(1+z)$ in the integrand due to redshifting of the photon energies.

In summary, the planned surveys with *Herschel* should be able to resolve into sources around 30-50% of the total IR dust emission, and thus a similar fraction of the dust-obscured massive star formation, over the history of the Universe.

8 CLUSTERING OF GALAXIES IN THE FAR-IR

The final topic we consider is the predicted clustering of galaxies detected in the far-IR by *Herschel*. In the GALFORM model,

the clustering of galaxies is determined (on large scales) by that of their host dark matter halos, and (on small scales) by the spatial distribution of galaxies within dark matter halos. Observational measurements of clustering for galaxies of different classes and luminosities can thus provide robust information about the masses of the dark halos hosting these galaxies. Such information is difficult to obtain in other ways, particularly for high redshift galaxies (for example, measurements of galaxy circular velocities do not probe the radii where most of the halo mass is, and so only weakly constrain halo masses). Clustering measurements can thus provide an essential test of the link between mass (mostly in dark matter) and light, which provides a fundamental test of the galaxy formation model.

We limit ourselves here to a few predictions for large-scale clustering, and defer a more detailed analysis of clustering properties to a future paper. On large scales, where the density fluctuations for the dark matter are still in the linear regime, the clustering of galaxies and halos can be described by a linear bias factor b , such that $\xi(r) = b^2 \xi_{dm}(r)$, where $\xi(r)$ is the 2-point correlation function for the galaxies or halos, and $\xi_{dm}(r)$ is that for the dark matter. We can calculate the bias, $b_{halo}(M, z)$, for halos as a function of halo mass and redshift using the analytical approximation of Sheth et al. (2001). We can then calculate the bias, $b_{gal}(L_{IR}, z)$, for galaxies of a specified IR luminosity as a mean of the halo bias, weighted by the distribution of host halo masses for galaxies of this luminosity and redshift. The latter information is provided by the semi-analytical model. We show the results of this calculation in the top panel of Fig. 21. We see from this that the clustering bias is predicted to depend only weakly on total IR luminosity over the range $10^9 \lesssim L_{IR} \lesssim 10^{11.5} h^{-2} L_{\odot}$, but to increase steeply at the highest luminosities. The weak dependence on IR luminosity stems from the weak correlation of IR luminosity with host halo mass, which was seen in Fig. 13. The bias at a given IR luminosity is seen to increase gradually with redshift, from $b \sim 1$ at $z = 0$, to $b \sim 2$ at $z = 3$, for the luminosity range where b is roughly constant.

By combining our analytical estimate of the bias with an estimate of the correlation function, $\xi_{dm}(r, z)$, of the dark matter, we can calculate the correlation function of the galaxies, $\xi_{gal}(r, L_{IR}, z) = b_{gal}^2(L_{IR}, z) \xi_{dm}(r, z)$. This estimate will be valid on scales large enough that the linear bias approximation is valid. We calculate the dark matter correlation function using the approximate analytical model of Smith et al. (2003), which allows for non-linear effects in the dark matter evolution. From this, we can calculate the correlation length, r_0 , which we define by $\xi(r_0) = 1$, and which provides a simple, directly measurable, characterization of how strongly a particular population of galaxies is clustered. This approach to calculating r_0 is valid provided $b \geq 1$, since then $\xi_{dm}(r_0) \leq 1$, and the dark matter is still approximately in the linear regime on the scale r_0 . We show our predictions for r_0 in the lower panel of Fig. 21. We see from this that, as for the bias, r_0 is almost independent of luminosity over the range $10^9 \lesssim L_{IR} \lesssim 10^{11.5} h^{-2} L_{\odot}$, but increases steeply for $L_{IR} \gtrsim 10^{11.5} h^{-2} L_{\odot}$. At a given luminosity, r_0 decreases with increasing redshift, but typically only gradually. For $10^9 \lesssim L_{IR} \lesssim 10^{11.5} h^{-2} L_{\odot}$, r_0 decreases from $r_0 \sim 5h^{-1} \text{Mpc}$ at $z = 0$ to $r_0 \sim 3h^{-1} \text{Mpc}$ at $z = 3$.

Viero et al. (2009) have estimated the clustering of galaxies in the SPIRE bands from the BLAST observations by measuring the angular power spectra of the total intensity maps. From this, they estimate a bias $b \sim 4$ for the galaxies responsible for the far-IR background, larger than the values typical in our model. However, their estimate of the bias relies on a model for the source redshift

distribution, and assumes that the bias is independent of both redshift and IR luminosity. The latter assumption seems unrealistic in the light of our own predictions for the bias shown in Fig. 21(a). We therefore do not make a more detailed comparison with their results.

Finally, in Fig. 22, we show simulated images of a slice through the universe at $z = 1$, $100h^{-1} \text{Mpc}$ wide by $10h^{-1} \text{Mpc}$ thick. These have been obtained by combining our semi-analytical model with the Millennium dark matter simulation (Springel et al. 2005), using the same method as in Orsi et al. (2008). In these images, the dark matter distribution is shown in green, while the positions and luminosities of the galaxies are shown as coloured blobs. For making these images, we have calculated the far-IR luminosities of galaxies using the simplified dust emission model described in Gonzalez et al. (2010), since running the GRASIL dust code separately on each galaxy in the Millennium simulation would not have been feasible computationally. In a future paper, we will present images calculated using a more accurate approximation to GRASIL based on Artificial Neural Nets (Almeida et al. 2009). The top two panels show galaxies selected based on their total IR luminosities, brighter than $10^{11} h^{-2} L_{\odot}$ and $10^{12} h^{-2} L_{\odot}$ respectively in the left and right panels. The lower left panel shows galaxies selected to have $100\mu\text{m}$ fluxes brighter than 2mJy , which is similar to the planned flux limit in the PEP GOODS-S survey. Finally, the lower right panel shows galaxies selected according to their dust-extincted rest-frame far-UV luminosities, with $M_{AB}(1500\text{\AA}) - 5 \log h < -21.2$. This absolute magnitude limit has been chosen because it corresponds to about the same SFR in a completely unextincted galaxy as does $L_{IR} = 10^{11} h^{-2} L_{\odot}$ in a completely extincted galaxy. Comparing the top left and lower right panels illustrates how incomplete surveys for star-forming galaxies can be if they use only observations in the rest-frame far-UV and ignore the far-IR.

9 SUMMARY AND CONCLUSIONS

We have used a detailed model of hierarchical galaxy formation and of the reprocessing of starlight by dust to make predictions for the evolution of the galaxy population at the far-infrared wavelengths ($60\text{--}670\mu\text{m}$) which will be probed by observations with the *Herschel* Space Observatory. We calculated galaxy formation in the framework of the ΛCDM model using the GALFORM semi-analytical model, which includes physical treatments of the hierarchical assembly of dark matter halos, shock-heating and cooling of gas, star formation, feedback from supernova explosions and photo-ionization of the IGM, galaxy mergers and chemical enrichment. We computed the IR luminosities and SEDs of galaxies using the GRASIL multi-wavelength spectrophotometric model, which computes the luminosities of the stellar populations in galaxies, and then the reprocessing of this radiation by dust, including radiative transfer through a two-phase dust medium, and a self-consistent calculation of the distribution of grain temperatures in each galaxy based on a local balance between heating and cooling.

Our galaxy formation model incorporates two different IMFs: quiescent star formation in galaxy disks occurs with a normal solar neighbourhood IMF, but star formation in starbursts triggered by galaxy mergers happens with a top-heavy $x = 0$ IMF. In a previous paper (Baugh et al. 2005), we found that the top-heavy IMF in bursts was required in order that the model reproduces the observed number counts of the faint sub-mm galaxies detected at $850\mu\text{m}$, which are typically ultra-luminous starbursts at $z \sim 2$, with total IR

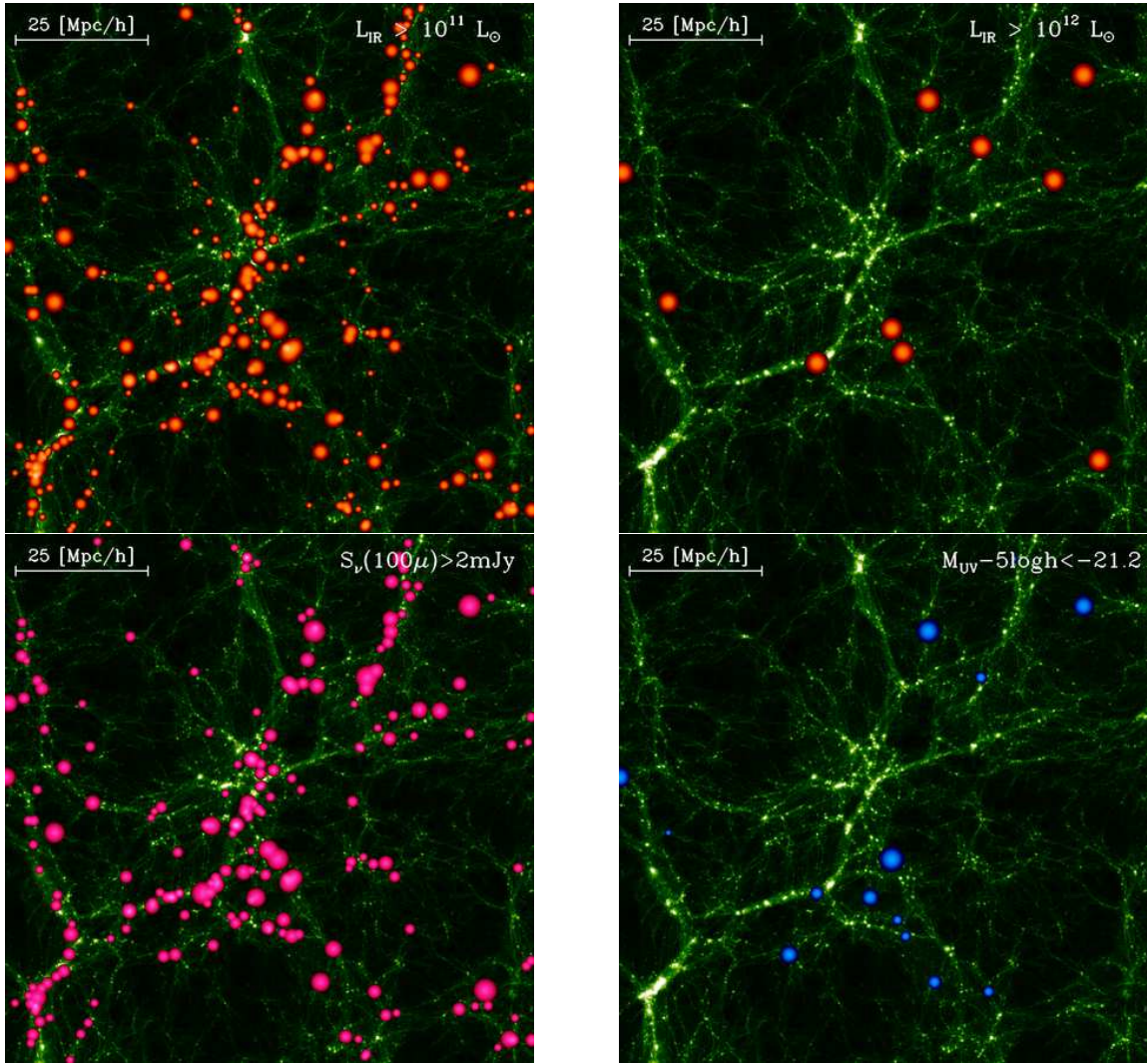


Figure 22. Images of a simulated slice of the universe $100h^{-1}\text{Mpc}$ wide and $10h^{-1}\text{Mpc}$ thick at $z = 1$. Each panel shows the same slice, with the dark matter density plotted in green, and with the galaxies plotted as coloured blobs, the blob size increasing with luminosity or flux. Each panel shows galaxies selected at a different wavelength and/or luminosity/flux. (a) $L_{\text{IR}} > 10^{11}h^{-2}L_{\odot}$. (b) $L_{\text{IR}} > 10^{12}h^{-2}L_{\odot}$. (c) $S_{\nu}(100\mu\text{m}) > 2\text{mJy}$. (d) $M_{\text{UV}} - 5\log h < -21.2$.

luminosities $L_{\text{IR}} \sim 10^{12} - 10^{13}L_{\odot}$. We subsequently found that the same model also reproduces the evolution of the galaxy population at mid-infrared wavelengths found by *Spitzer* (Lacey et al. 2008). We have used the same model, with identical parameters, to make predictions for *Herschel* in the present paper.

We began (§3) by showing the predicted evolution of the galaxy luminosity function at far-IR wavelengths. This brightens by a factor ~ 10 going back from $z = 0$ to $z \sim 3$, reflecting both the evolution of star formation rates in galaxies and the increasing importance of the top-heavy burst mode with increasing redshift. We next (§4) presented predictions for galaxy number counts as functions of flux in the *Herschel* PACS and SPIRE imaging bands (covering the wavelength range $70\text{--}500\mu\text{m}$). We calculated the confusion limits for the *Herschel* bands, and found that source confusion is likely to be a serious problem for all of the deepest cosmological surveys planned (PEP, GOODS-*Herschel* and HERMES) (except at $70\mu\text{m}$). The number of faint galaxies which can be resolved in these surveys will depend dramatically on whether or not the confusion limit can be circumvented, e.g. by using multi-wavelength data. We also investigated the predicted redshift distributions in

these deep cosmological surveys and in the wide-area ATLAS survey. We found that the deep surveys should reach median redshifts $\sim 1 - 1.8$, depending on the wavelength and on whether it is possible in practice to probe sources fainter than the confusion limit. The highest median redshift ($1.4\text{--}1.8$, depending on confusion) should be attained in the HERMES survey at $500\mu\text{m}$. For the ATLAS survey, the median redshift should be $0.2\text{--}0.4$, with the highest value at $250\mu\text{m}$. At the faintest fluxes and highest redshifts, the galaxy source population is predicted to be dominated by starbursts.

Following on from the predictions for source counts and redshifts, in §5 we showed what the model predicts for some of the basic physical properties of galaxies detected in different *Herschel* bands as functions of flux and redshift. As expected, at each redshift there are nearly linear correlations between the fluxes in different bands and the total IR luminosity L_{IR} (integrated over the wavelength range $8\text{--}1000\mu\text{m}$). On the other hand, the relation between the total star formation rate SFR and flux shows more non-linearity, principally due to the different IMFs assumed in starburst galaxies (which dominate at high luminosity) and quiescent galaxies (which dominate at low luminosity). The deep-

est surveys should resolve galaxies with $L_{IR} \gtrsim 10^{11} h^{-2} L_{\odot}$ at $z = 1$ and $L_{IR} \gtrsim 10^{12} h^{-2} L_{\odot}$ at $z = 2$, corresponding to SFRs $\gtrsim 10 - 100 h^{-1} M_{\odot} \text{yr}^{-1}$. The stellar and dark halo masses of *Herschel* galaxies show much weaker correlations with flux and redshift, and with much more scatter, in large part because of the role of starbursts triggered by galaxy mergers. In the deep surveys at $z = 1 - 2$, the typical *Herschel*-detected galaxy should have a stellar mass $\sim 10^{10} h^{-1} M_{\odot}$ and a halo mass $\sim 10^{12} h^{-1} M_{\odot}$, and a typical gas mass $\sim 10^{10} h^{-1} M_{\odot}$. Finally, the morphologies of the galaxies detected in the *Herschel* cosmological surveys should be quite mixed, ranging from highly bulge-dominated to highly disk dominated systems, reflecting our assumption that starbursts can be triggered by both major and minor galaxy mergers.

Since our model is a multi-wavelength model, we used it in §6 to predict what should be the fluxes at other wavelengths (ranging from the far-UV to the radio) of galaxies detected in *Herschel* surveys. Follow-up data at other wavelengths will be essential both to determine redshifts of *Herschel* sources and to investigate their physical properties. Specifically, we presented predictions for the *GALEX* NUV band, the SDSS *r* band, the *Spitzer* 3.6 and $24\mu\text{m}$ bands, the *SCUBA* $850\mu\text{m}$ band and finally the 1.4GHz radio flux.

One of the primary goals of *Herschel* will be to unveil the history of dust-obscured star formation in the Universe. Therefore, in §7 we presented the predictions of our model for the cosmic star formation history and for the evolution of the cosmic emissivity of galaxies in the UV and the mid/far-IR. Our model predicts that, over the history of the Universe, about 90% of the UV radiation from massive young stars has been reprocessed by dust into the mid/far-IR wavelength range. We used our model to investigate what fraction of the total energy emitted by dust heated by stars over the history of the Universe should be resolved into galaxies by different planned *Herschel* surveys. We find that the fraction of the total IR emission resolved in this way should be $\sim 50\%$ if individual sources can be resolved all the way down to the nominal survey flux limits set by signal-to-noise, but only $\sim 30\%$ if source confusion sets a hard limit. Of the currently planned surveys, those at 100 or $160\mu\text{m}$ should be able to resolve the largest fraction of the time-integrated IR emission. This then implies that *Herschel* should resolve a similar fraction of the massive star formation over the history of the Universe (roughly $m \gtrsim 5M_{\odot}$, since these stars are responsible for most of the UV heating of dust grains). Lower-mass stars make only a small contribution to powering the mid/far-IR emission from dust, so determining the total SFRs from *Herschel* observations relies on extrapolating to lower masses ($m \lesssim 5M_{\odot}$) based on an assumed IMF. If, as assumed in our model, the IMF is different in different types of galaxy (quiescent *vs* starburst), then estimating total SFRs from IR data becomes much more complicated and uncertain, but estimates of the SFRs in high-mass stars should be much more robust.

Finally, in §8, we briefly investigated the predicted clustering of *Herschel* galaxies. We found that the typical galaxies in *Herschel* cosmological surveys should have a modest clustering bias ($b \sim 1 - 2$) relative to the dark matter, with correlation lengths $r_0 \sim 3 - 5 h^{-1} \text{Mpc}$ (in comoving units), except at the highest luminosities ($L_{IR} \gtrsim 10^{12} h^{-2} L_{\odot}$). Measurements of the clustering in *Herschel* surveys will provide an essential test of the relation between galactic star formation rates and halo masses predicted by our galaxy formation model.

ACKNOWLEDGEMENTS

We thank the referee Steve Eales for a helpful and positive report. This work was supported in part by the Science and Technology Facilities Council rolling grant to the ICC. CSF acknowledges a Royal Society Wolfson Research Grant Award, and CMB a Royal Society University Research Fellowship. AO is supported by a Gemini Fellowship from the STFC. AJB acknowledges the support of the Gordon and Betty Moore Foundation.

REFERENCES

- Abazajian K. N., Adelman-McCarthy J. K., Agüeros M. A., Allam S. S., Allende Prieto C., An D., Anderson K. S. J., Anderson et al., 2009, *ApJS*, 182, 543
- Almaini O., Lawrence A., Boyle B. J., 1999, *MNRAS*, 305, L59
- Almeida C., Baugh C. M., Lacey C. G., Frenk C. S., Granato G. L., Silva L., Bressan A., 2009, *ArXiv e-prints*
- Baugh C. M., 2006, *Reports on Progress in Physics*, 69, 3101
- Baugh C. M., Lacey C. G., Frenk C. S., Granato G. L., Silva L., Bressan A., Benson A. J., Cole S., 2005, *MNRAS*, 356, 1191
- Becker R. H., White R. L., Helfand D. J., 1995, *ApJ*, 450, 559
- Beckwith S. V. W., Stiavelli M., Koekemoer A. M., Caldwell J. A. R., Ferguson H. C., Hook R., Lucas R. A., Bergeron et al., 2006, *AJ*, 132, 1729
- Bower R. G., Benson A. J., Malbon R., Helly J. C., Frenk C. S., Baugh C. M., Cole S., Lacey C. G., 2006, *MNRAS*, 370, 645
- Bressan A., Granato G. L., Silva L., 1998, *A&A*, 332, 135
- Bressan A., Panuzzo P., Buson L., Clemens M., Granato G. L., Rampazzo R., Silva L., Valdes J. R., Vega O., Danese L., 2006, *ApJ*, 639, L55
- Bressan A., Silva L., Granato G. L., 2002, *A&A*, 392, 377
- Calzetti D., Bohlin R. C., Kinney A. L., Storchi-Bergmann T., Heckman T. M., 1995, *ApJ*, 443, 136
- Cattaneo A., Dekel A., Devriendt J., Guiderdoni B., Blaizot J., 2006, *MNRAS*, 370, 1651
- Chambers K. C., 2006, *Mission Concept Statement for PS1 Pan-STARRS Telescope #1*. Tech. Rep. PSDC-230-002-00, Institute for Astronomy, University of Hawaii
- Chapman S. C., Blain A. W., Smail I., Ivison R. J., 2005, *ApJ*, 622, 772
- Chary R., Casertano S., Dickinson M. E., Ferguson H. C., Eisenhardt P. R. M., Elbaz D., Grogin N. A., Moustakas L. A., Reach W. T., Yan H., 2004, *ApJS*, 154, 80
- Chavez M., Bertone E., Morales-Hernandez J., Bressan A., 2009, *ApJ*, 700, 694
- Clemens M. S., Bressan A., Panuzzo P., Rampazzo R., Silva L., Buson L., Granato G. L., 2009, *MNRAS*, 392, 982
- Cole S., Lacey C. G., Baugh C. M., Frenk C. S., 2000, *MNRAS*, 319, 168
- Condon J. J., 1974, *ApJ*, 188, 279
- Condon J. J., Cotton W. D., Greisen E. W., Yin Q. F., Perley R. A., Taylor G. B., Broderick J. J., 1998, *AJ*, 115, 1693
- Croton D. J., Springel V., White S. D. M., De Lucia G., Frenk C. S., Gao L., Jenkins A., Kauffmann G., Navarro J. F., Yoshida N., 2006, *MNRAS*, 365, 11
- Devlin M. J., Ade P. A. R., Aretxaga I., Bock J. J., Chapin E. L., Griffin M., Gundersen J. O., Halpern et al., 2009, *Nature*, 458, 737
- Devriendt J. E. G., Guiderdoni B., 2000, *A&A*, 363, 851

- Dickinson M., FIDEL team, 2007, in *Bulletin of the American Astronomical Society*, Vol. 38, *Bulletin of the American Astronomical Society*, pp. 822–+
- Dickinson M., Giavalisco M., The Goods Team, 2003, in *The Mass of Galaxies at Low and High Redshift*, Bender R., Renzini A., eds., pp. 324–+
- Dole H., Lagache G., Puget J.-L., Caputi K. I., Fernández-Conde N., Le Floc'h E., Papovich C., Pérez-González et al., 2006, *A&A*, 451, 417
- Dole H., Rieke G. H., Lagache G., Puget J.-L., Alonso-Herrero A., Bai L., Blaylock M., Egami et al., 2004, *ApJS*, 154, 93
- Elbaz D., 2005, *Space Science Reviews*, 119, 93
- Elmegreen B. G., 2009, in *The Evolving ISM in the Milky Way and Nearby Galaxies*
- Fardal M. A., Katz N., Weinberg D. H., Davé R., 2007, *MNRAS*, 379, 985
- Fernandez-Conde N., Lagache G., Puget J.-L., Dole H., 2008, *A&A*, 481, 885
- Figer D. F., Kim S. S., Morris M., Serabyn E., Rich R. M., McLean I. S., 1999, *ApJ*, 525, 750
- Fixsen D. J., Dwek E., Mather J. C., Bennett C. L., Shafer R. A., 1998, *ApJ*, 508, 123
- Fomalont E. B., Kellermann K. I., Cowie L. L., Capak P., Barger A. J., Partridge R. B., Windhorst R. A., Richards E. A., 2006, *ApJS*, 167, 103
- Fontanot F., Monaco P., Silva L., Grazian A., 2007, *MNRAS*, 382, 903
- González J. E., Lacey C. G., Baugh C. M., Frenk C. S., Benson A. J., 2009, *MNRAS*, 397, 1254
- Gonzalez J. E., Lacey C. G., Baugh C. M., Frenk C. S., Benson A. J., 2010. In preparation
- Granato G. L., De Zotti G., Silva L., Bressan A., Danese L., 2004, *ApJ*, 600, 580
- Granato G. L., Lacey C. G., Silva L., Bressan A., Baugh C. M., Cole S., Frenk C. S., 2000, *ApJ*, 542, 710
- Harayama Y., Eisenhauer F., Martins F., 2008, *ApJ*, 675, 1319
- Hauser M. G., Arendt R. G., Kelsall T., Dwek E., Odegard N., Weiland J. L., Freudenreich H. T., Reach et al., 1998, *ApJ*, 508, 25
- Helly J. C., Cole S., Frenk C. S., Baugh C. M., Benson A., Lacey C., 2003, *MNRAS*, 338, 903
- Hopkins A. M., Afonso J., Chan B., Cram L. E., Georgakakis A., Mobasher B., 2003, *AJ*, 125, 465
- Hughes D. H., Serjeant S., Dunlop J., Rowan-Robinson M., Blain A., Mann R. G., Ivison R., Peacock et al., 1998, *Nature*, 394, 241
- Huynh M. T., Frayer D. T., Mobasher B., Dickinson M., Chary R.-R., Morrison G., 2007, *ApJ*, 667, L9
- Kashikawa N., Shimasaku K., Yasuda N., Ajiki M., Akiyama M., Ando H., Aoki K., Doi et al., 2004, *PASJ*, 56, 1011
- Kennicutt Jr. R. C., 1983, *ApJ*, 272, 54
- Kroupa P., 2001, *MNRAS*, 322, 231
- Lacey C. G., Baugh C. M., Frenk C. S., Silva L., Granato G. L., Bressan A., 2008, *MNRAS*, 385, 1155
- Lagache G., Dole H., Puget J.-L., 2003, *MNRAS*, 338, 555
- Lagos C. D. P., Cora S. A., Padilla N. D., 2008, *MNRAS*, 388, 587
- Larson R. B., 1998, *MNRAS*, 301, 569
- , 2005, *MNRAS*, 359, 211
- Le Delliou M., Lacey C., Baugh C. M., Guiderdoni B., Bacon R., Courtois H., Sousbie T., Morris S. L., 2005, *MNRAS*, 357, L11
- Le Delliou M., Lacey C. G., Baugh C. M., Morris S. L., 2006, *MNRAS*, 365, 712
- Le Floc'h E., Papovich C., Dole H., Bell E. F., Lagache G., Rieke G. H., Egami E., Pérez-González et al., 2005, *ApJ*, 632, 169
- Li A., Draine B. T., 2001, *ApJ*, 554, 778
- Lilly S. J., Le Fevre O., Hammer F., Crampton D., 1996, *ApJ*, 460, L1+
- Lonsdale C., Polletta M. d. C., Surace J., Shupe D., Fang F., Xu C. K., Smith H. E., Siana et al., 2004, *ApJS*, 154, 54
- Lonsdale C. J., Smith H. E., Rowan-Robinson M., Surace J., Shupe D., Xu C., Oliver S., Padgett et al., 2003, *PASP*, 115, 897
- Madau P., Ferguson H. C., Dickinson M. E., Giavalisco M., Steidel C. C., Fruchter A., 1996, *MNRAS*, 283, 1388
- Maness H., Martins F., Trippe S., Genzel R., Graham J. R., Sheehy C., Salaris M., Gillessen et al., 2007, *ApJ*, 669, 1024
- Marsden G., Ade P. A. R., Bock J. J., Chapin E. L., Devlin M. J., Dicker S. R., Griffin M., Gundersen et al., 2009, *ApJ*, 707, 1729
- McCraday N., Gilbert A. M., Graham J. R., 2003, *ApJ*, 596, 240
- Meurer G. R., Heckman T. M., Calzetti D., 1999, *ApJ*, 521, 64
- Meurer G. R., Heckman T. M., Leitherer C., Kinney A., Robert C., Garnett D. R., 1995, *AJ*, 110, 2665
- Meurer G. R., Wong O. I., Kim J. H., Hanish D. J., Heckman T. M., Werk J., Bland-Hawthorn J., Dopita et al., 2009, *ApJ*, 695, 765
- Mollá M., García-Vargas M. L., Bressan A., 2009, *MNRAS*, 398, 451
- Monaco P., Fontanot F., Taffoni G., 2007, *MNRAS*, 375, 1189
- Morrissey P., Conrow T., Barlow T. A., Small T., Seibert M., Wyder T. K., Budavári T., Arnouts et al., 2007, *ApJS*, 173, 682
- Mortier A. M. J., Serjeant S., Dunlop J. S., Scott S. E., Ade P., Alexander D., Almaini O., Aretxaga et al., 2005, *MNRAS*, 363, 563
- Nagashima M., Lacey C. G., Baugh C. M., Frenk C. S., Cole S., 2005a, *MNRAS*, 358, 1247
- Nagashima M., Lacey C. G., Okamoto T., Baugh C. M., Frenk C. S., Cole S., 2005b, *MNRAS*, 363, L31
- Negrello M., Perrotta F., González-Nuevo J., Silva L., de Zotti G., Granato G. L., Baccigalupi C., Danese L., 2007, *MNRAS*, 377, 1557
- Orsi A., Lacey C. G., Baugh C. M., Infante L., 2008, *MNRAS*, 391, 1589
- Parra R., Conway J. E., Diamond P. J., Thrall H., Lonsdale C. J., Lonsdale C. J., Smith H. E., 2007, *ApJ*, 659, 314
- Patanchon G., Ade P. A. R., Bock J. J., Chapin E. L., Devlin M. J., Dicker S. R., Griffin M., Gundersen et al., 2009, *ApJ*, 707, 1750
- Paumard T., Genzel R., Martins F., Nayakshin S., Beloborodov A. M., Levin Y., Trippe S., Eisenhauer et al., 2006, *ApJ*, 643, 1011
- Pérez-González P. G., Rieke G. H., Egami E., Alonso-Herrero A., Dole H., Papovich C., Blaylock M., Jones et al., 2005, *ApJ*, 630, 82
- Pérez-González P. G., Rieke G. H., Villar V., Barro G., Blaylock M., Egami E., Gallego J., Gil de Paz et al., 2008, *ApJ*, 675, 234
- Puget J.-L., Abergel A., Bernard J.-P., Boulanger F., Burton W. B., Desert F.-X., Hartmann D., 1996, *A&A*, 308, L5+
- Rieke G. H., Loken K., Rieke M. J., Tamblyn P., 1993, *ApJ*, 412, 99
- Rowan-Robinson M., 2001, *ApJ*, 549, 745
- , 2009, *MNRAS*, 394, 117
- Sheth R. K., Mo H. J., Tormen G., 2001, *MNRAS*, 323, 1
- Silva L., De Zotti G., Granato G. L., Maiolino R., Danese L., 2005, *MNRAS*, 357, 1295
- Silva L., Granato G. L., Bressan A., Danese L., 1998, *ApJ*, 509, 103

- Smail I., Ivison R. J., Blain A. W., 1997, *ApJ*, 490, L5+
- Smith R. E., Peacock J. A., Jenkins A., White S. D. M., Frenk C. S., Pearce F. R., Thomas P. A., Efstathiou et al., 2003, *MNRAS*, 341, 1311
- Soifer B. T., Helou G., Werner M., 2008, *ARA&A*, 46, 201
- Soifer B. T., Neugebauer G., Houck J. R., 1987, *ARA&A*, 25, 187
- Solomon P. M., Vanden Bout P. A., 2005, *ARA&A*, 43, 677
- Springel V., White S. D. M., Jenkins A., Frenk C. S., Yoshida N., Gao L., Navarro J., Thacker et al., 2005, *Nature*, 435, 629
- Steidel C. C., Adelberger K. L., Giavalisco M., Dickinson M., Pettini M., 1999, *ApJ*, 519, 1
- Stolte A., Brandner W., Grebel E. K., Lenzen R., Lagrange A.-M., 2005, *ApJ*, 628, L113
- Swinbank A. M., Lacey C. G., Smail I., Baugh C. M., Frenk C. S., Blain A. W., Chapman S. C., Coppin et al., 2008, *MNRAS*, 391, 420
- Väisänen P., Tollestrup E. V., Fazio G. G., 2001, *MNRAS*, 325, 1241
- van Dokkum P. G., 2008, *ApJ*, 674, 29
- Vega O., Clemens M. S., Bressan A., Granato G. L., Silva L., Panuzzo P., 2008, *A&A*, 484, 631
- Vega O., Silva L., Panuzzo P., Bressan A., Granato G. L., Chavez M., 2005, *MNRAS*, 364, 1286
- Viero M. P., Ade P. A. R., Bock J. J., Chapin E. L., Devlin M. J., Griffin M., Gundersen J. O., Halpern et al., 2009, *ApJ*, 707, 1766
- Wright E. L., Eisenhardt P. R. M., Mainzer A. K., Kirkpatrick J. D., Cohen M., 2007, in *American Institute of Physics Conference Series*, Vol. 943, *The Science Opportunities of the Warm Spitzer Mission Workshop*, Storrie-Lombardi L. J., Silbermann N. A., eds., pp. 242–247